

FUSE OBSERVATIONS OF THE SMC 16 DAY WOLF-RAYET BINARY SANDULEAK 1 (WO4+O4): ATMOSPHERIC ECLIPSES AND COLLIDING STELLAR WINDS¹

NICOLE ST-LOUIS AND ANTHONY F. J. MOFFAT

Département de physique, Université de Montréal, Montréal, QC H3C 3J7, Canada; and Observatoire du mont Mégantic;
stlouis@astro.umontreal.ca, moffat@astro.umontreal.ca

SERGEY MARCHENKO

Department of Physics and Astronomy, Western Kentucky University, Bowling Green,
KY 42101-3576; sergey@astro.wku.edu

AND

JULIAN MARK PITTARD

Department of Physics and Astronomy, University of Leeds, Woodhouse Lane,
Leeds LS2 9JT, England, UK; jmp@ast.leeds.ac.uk

Received 2004 June 28; accepted 2005

ABSTRACT

In this paper we present the results of a *FUSE* monitoring campaign of the SMC WO4+O4 V Wolf-Rayet binary Sanduleak 1. Our 18 spectra obtained during a little more than one orbital cycle in 2000 October combined with four archival spectra show variability in the S VI, C III, C IV, and O VI P Cygni profiles, which we attribute to emission from the shock cone resulting from the collision between the two strong winds and to atmospheric eclipses of the O star continuum light by the W-R wind. All the lines vary in concert indicating that the cooling is such that even lines such as the O VI $\lambda\lambda 1032, 1038$ doublet form in the linear part of the cone. We have also applied both a simple geometrical model and profile fits, including emission from the normal wind, extra emission from the shock cone, and the atmospheric eclipse. Adopting an orbital inclination of $\sim 40^\circ$, we deduce a total cone opening angle of $\sim 80^\circ$ and a streaming velocity for the gas along the shock cone of $\sim 3000 \text{ km s}^{-1}$. The luminosity ratio required to fit our spectra is $L_O/L_{W-R} = 3.5$, and the stellar radii are 3.5 and 12 R_\odot , respectively, for the W-R and O stars. We also present radiative driving models for this binary system having two massive stars with strong winds and discuss radiative inhibition and braking effects. In particular, we address the coupling of the O star radiation with the W-R star wind. Finally, we present a PICA hydrodynamic colliding-wind model for Sand 1. We find an opening angle for the shock cone similar to that deduced from the line-profile fitting, but significantly longer cooling lengths along the shock cone. However, the model reveals some cold gas that is stripped off the O4 surface and mixed with the hotter WO4 material, thereby accelerating its cooling. This could very well explain why shorter cooling lengths are inferred from the profile fits.

Subject headings: binaries: spectroscopic — stars: individual (Sanduleak 1) — stars: winds, outflows — stars: Wolf-Rayet

1. THE ENCOUNTER OF TWO MASSIVE OUTFLOWS

The study of the gravitational interaction between stars in a binary system has long been proven to be the foremost method to estimate fundamental stellar parameters. The incessant dance of spectral lines as the stars orbit each other, occasionally combined with light variations caused by core eclipses, are the direct manifestation of the simple physical processes involved, and their interpretation insures nearly direct access to quantities such as mass and radius. However, when studying binaries containing massive stars, one must contend with an additional element: the interaction of the dense stellar winds.

Classical Population I Wolf-Rayet (W-R) stars, the evolved descendants of massive O stars, possess the most energetic, sustained winds of all (massive) stars. In view of their short lifetime (~ 0.6 Myr; Maeder & Meynet 1994), when they are in binaries they are generally accompanied by much longer lived (\sim a factor of 10) O stars. The rapid outflows from two hot, massive

stars in a binary system will undeniably interact, generating two striking effects. First, since the wind mean free path is short and the wind collision is supersonic, a shock front will form at the location where the perpendicular component of the vectorial momentum fluxes of the two stars cancel. In the case of a W-R+O binary, the resulting shock structure takes roughly the shape of a cone with a rounded apex that is wrapped around the weaker wind O star.

Considering typical mass-loss rates for O ($\dot{M} \sim 3 \times 10^{-6} M_\odot \text{ yr}^{-1}$; Puls et al. 1996) and W-R stars ($\dot{M} \sim 2.5 \times 10^{-5} M_\odot \text{ yr}^{-1}$; Nugis et al. 1998), as well as typical wind terminal velocities for O ($v_\infty \sim 2200 \text{ km s}^{-1}$; Prinja et al. 1990) and W-R ($\sim 1800 \text{ km s}^{-1}$; Nugis et al. 1998) stars, the energetic collision at the bow shock head will heat the gas to several million degrees, producing copious amounts of X-rays. The hot gas then flows along the shock cone and cools radiatively, thereby emitting light in lines of successively decreasing ionization/excitation potential along the way. This line emission will be superposed on the normal line emission from the W-R and, if strong enough, O star winds to varying degrees, depending on the details of each flow. As a function of orbital phase, the cone revolves with the system and is thus viewed from different angles. The excess emission is thereby displaced

¹ Based on observations made with the NASA-CNES-CSA *Far Ultraviolet Spectroscopic Explorer*. *FUSE* is operated for NASA by Johns Hopkins University under NASA contract NAS-32985.

by the associated Doppler shift (i.e., due to the vector sum of the orbit and the outflow).

The other important physical process that takes place is the so-called selective atmospheric eclipse. This occurs when the continuum light of the O star is absorbed in lines of common ions by W-R wind material in the line of sight. The shape of the resulting absorption profile, which will also be superposed on the normal wind emission lines, depends on the velocity and opacity distribution of the gas that the light encounters along the line of sight (Auer & Koenigsberger 1994). The study of this absorption profile provides valuable information on the density and velocity structures of the W-R wind.

The excess emission from the shock cone resulting from colliding stellar winds and selective atmospheric eclipses will produce significant phase-dependent variability of the observed spectra. The study of these changes and their decomposition and comparison with theoretical predictions will lead to better constraints on the geometry of the shock cone and subsequently on W-R stellar-wind and binary-system parameters.

The *Far Ultraviolet Spectroscopic Explorer* (*FUSE*), described by Moos et al. (2000) and Sahnou et al. (2000), is ideal for studying the spectral variability generated by atmospheric eclipses and the shock cone from the wind-wind collision. Indeed, its wavelength region encompasses lines of several ionization states of ions commonly found in hot-star winds. In view of the well-known ionization stratification of W-R winds (Herald et al. 2000), this wealth of lines will allow us to simultaneously probe the W-R outflow at different radial distances from the star. Also, it will be possible to study emission from various positions along the wind-wind interaction shock cone, thereby allowing a more detailed mapping of its structure. In particular, the O VI $\lambda\lambda 1032, 1038$ doublet might be expected to be formed relatively close to the bow shock head, where the X-ray emission is expected to arise.

To further our understanding of these effects, we chose to use *FUSE* to observe the W-R+O binary Sanduleak 1, which is the brightest member of the SMC open cluster NGC 602c. This cluster was studied most recently by Massey & DeGioia-Eastwood (2000), who estimated its age to be ~ 3 Myr. It contains stars as hot as O6.5, excluding the O companion of this W-R+O binary. Depending on the adopted definition of the WO subclass, the W-R component has been classified WO4 (Kingsburgh et al. 1995) or WO3 (Crowther et al. 1998). The spectral type of the O component is still somewhat subject to controversy; it was classified O4 by Breysacher & Westerlund (1978) and O4 V by Moffat et al. (1985), while Barlow & Hummer (1982) and Kingsburgh et al. (1995) found a later spectral type of O7. Recently, Massey & DeGioia-Eastwood (2000) obtained a new spectrum of this system, and they adopt an O4 V spectral type for the O star component, which we also do here. The O4 V type is not incompatible with that of the earliest stars in NGC 602c in view of its sparse nature.

The wind of the W-R member of this binary system is one of the fastest known ($v_\infty = 4200 \text{ km s}^{-1}$; Kingsburgh et al. 1995). Given the early type of the O companion, it is therefore possible that the effects of the interaction between the two winds will be extreme and therefore more obvious to study. This project is part of a wider *FUSE* study including other W-R+O binaries showing similar colliding winds and atmospheric eclipse effects. Eventually we intend to contrast the results for this system with those of other systems of different spectral types and orbital period and in different galaxies (SMC vs. LMC vs. the Galaxy). This will be limited, however, due to the severe effects

of interstellar extinction in the *FUSE* UV wavelength range and the resulting reduction in the number of (mainly Galactic) suitable candidates.

In § 2 we describe our observations and the data analysis we have carried out, while § 3 presents the observed spectral variability. The analysis can be found in § 4 and conclusions in § 5.

2. THE *FUSE* OBSERVATIONS

We have secured 18 *FUSE* spectra of Sand 1 between 2000 September 26 and October 13 in the Cycle 1 observing period. We have also added to this study four archival spectra obtained between 2000 October 6 and 11, which were discussed in detail in a different context by Hoopes et al. (2002).

The spectra were obtained in photon address (time-tag [TTAG]) mode through the large aperture ($30'' \times 30''$, LWRS) and span a broad wavelength range. *FUSE* comprises four co-aligned telescopes feeding four Rowland circle spectrographs, each with a spectral resolving power of $\sim 20,000$. Two of these channels cover shorter ultraviolet wavelengths (SiC1 and SiC2; 905–1100 Å), and two cover longer ultraviolet wavelengths (LiF1 and LiF2; 1000–1187 Å). As the photon-counting detectors are divided into two segments (A and B), each *FUSE* exposure therefore consists of eight separate data sets.

The log of the observations is presented in Table 1, which gives the program identification number, the spectrum number, the date and time at the beginning of the exposure, as well as the corresponding mean Heliocentric Julian Date and the exposure time of each individual observation. The majority of these observations consisted of two or three consecutive exposures, which we have combined to produce better quality spectra. The last column of Table 1 gives the orbital phase calculated with the ephemeris of Bartzakos et al. (2001).

Each individual raw exposure was run through the standard *FUSE* calibration pipeline (CALFUSE ver. 2.3.0). This version of the software performs several corrections to the data. First, it removes photon events recorded during South Atlantic Anomaly and low Earth limb angle pointings. Then it corrects for various photon-shift effects: first is the so-called gain sag, which is caused by loss in detector efficiency after prolonged exposures. Photon shifts caused by the rotation of the grating as a function of time and by the motion of the satellite around the Earth (and of course the Earth around the Sun) are also allowed for, to produce a heliocentric velocity scale. The second step is to remove event bursts; these are large count rate surges occurring on a well-defined but complex region of the *FUSE* detectors. These bursts are easy to identify and are removed from the data. The pipeline also applies a jitter correction required when a loss of pointing due to a slow drift occurs during an observation. The next step is to allow for bad pixels by flagging dead zones and regions beyond the active area of the detector. Then the background consisting of dark counts and scattered light is subtracted and the image is divided by the flat field. The last improvements applied to the two-dimensional image are corrections for detector distortion and spectrograph astigmatism. Finally, the one-dimensional spectrum is extracted via an optimal-extraction algorithm. Dead-time corrections due to detector electronics and to the Instrument Data System (IDS) computer are made. The spectra are then wavelength- and flux-calibrated (using time-dependent calibration files), resulting in eight one-dimensional spectra in the heliocentric reference frame.

As noted above, most *FUSE* observations consist of two or three separate exposures. Since we do not require the high

TABLE 1
LOG OF *FUSE* OBSERVATIONS OF SAND 1

Program ID Number ^a	Spectrum Number	Start Date	Start Time (UT)	Julian Date −2,451,800	Exposure Time (s)	Orbital Phase ^b
A12302.....	63	2000 Sep 26	08:37	13.86	2296	0.56
A12302.....	64-1	2000 Sep 27	06:15	14.76	781	0.61
A12302.....	64-2	2000 Sep 27	05:06	14.71	550	0.61
A12302.....	64-3	2000 Sep 27	06:37	14.78	960	0.62
A12302.....	65-1	2000 Sep 29	05:35	15.73	531	0.67
A12302.....	65-2	2000 Sep 28	06:00	15.75	811	0.67
A12302.....	65-3	2000 Sep 28	07:14	15.80	2257	0.68
A12302.....	66	2000 Sep 29	16:35	17.19	4038	0.76
A12302.....	67-1	2000 Sep 30	17:37	18.23	1977	0.82
A12302.....	67-2	2000 Sep 30	19:20	18.31	1701	0.83
A12302.....	68	2000 Oct 2	06:11	19.76	2061	0.91
A12302.....	81-1	2000 Oct 2	19:40	20.32	1591	0.95
A12302.....	81-2	2000 Oct 2	21:23	20.39	1310	0.95
A12302.....	69-1	2000 Oct 4	00:07	21.50	1067	0.02
A12302.....	69-2	2000 Oct 4	01:51	21.58	848	0.02
A12302.....	69-3	2000 Oct 4	03:24	21.64	1215	0.03
A12302.....	70-1	2000 May 10	09:11	22.88	1973	0.10
A12302.....	70-2	2000 May 10	10:49	22.95	203	0.11
P10306.....	02-1	2000 Oct 6	13:30	24.06	1890	0.17
P10306.....	02-2	2000 Oct 6	15:09	24.13	1920	0.18
P10306.....	02-3	2000 Oct 6	16:48	24.20	1931	0.18
A12302.....	71-1	2000 Oct 6	23:45	24.49	1188	0.20
A12302.....	71-2	2000 Oct 7	01:24	24.56	1129	0.20
A12302.....	72-1	2000 Oct 7	23:02	25.46	1570	0.26
A12302.....	72-2	2000 Oct 8	00:43	25.53	1413	0.26
A12302.....	73-1	2000 Oct 8	20:35	26.36	1929	0.31
A12302.....	73-2	2000 Oct 8	22:17	26.43	1728	0.32
A12302.....	74-1	2000 Oct 9	21:34	27.40	1938	0.37
A12302.....	74-2	2000 Oct 9	23:17	27.47	1659	0.38
P10306.....	04	2000 Oct 10	02:26	27.60	4102	0.39
P10306.....	01-1	2000 Oct 10	07:28	27.81	2001	0.40
P10306.....	01-2	2000 Oct 10	08:30	27.85	4521	0.40
P10306.....	01-3	2000 Oct 10	10:18	27.93	345	0.41
A12302.....	75	2000 Oct 10	22:35	28.44	2071	0.44
P10306.....	03	2000 Oct 11	05:09	28.71	4885	0.45
A12302.....	76	2000 Oct 11	21:50	29.41	4560	0.50
A12302.....	77-1	2000 Oct 12	09:26	29.89	2431	0.52
A12302.....	77-2	2000 Oct 12	10:38	29.94	4531	0.53
A12302.....	79-1	2000 Oct 13	07:06	30.80	2071	0.58
A12302.....	79-2	2000 Oct 13	08:08	30.84	4560	0.58
A12302.....	79-3	2000 Oct 13	09:55	30.91	1919	0.59
A12302.....	78-1	2000 Oct 13	20:26	31.35	4531	0.61
A12302.....	78-2	2000 Oct 13	22:05	31.42	1419	0.62

^a The data are archived in the Multimission Archive of the Space Telescope Institute (MAST).

^b Based on the ephemeris of Bartzakos et al. (2001), $P = 16.633$ days, and $E_0 = \text{HJD } 2,446,032.9$.

temporal resolution of such close groups of spectra, we aligned the two or three separate exposures using the plethora of interstellar lines, in particular of H_2 , present in the *FUSE* wavelength range. Using the exposure time as a weighting factor, the various exposures were then combined to produce one individual observation. A total of 22 such spectra result.

3. The *FUSE* spectra

3.1. Time-averaged Spectra

The *FUSE* wavelength region encompasses several key intrinsic spectral lines from both the O and W-R stars. Based on the *FUSE* atlas of Walborn et al. (2002) for O stars in the SMC and LMC, we expect the strongest features for an O4–O7 V star to be $\text{S VI } \lambda\lambda 933, 945$ and $\text{O VI } \lambda\lambda 1032, 1038$ P Cygni profiles

and a $\text{C III } \lambda 977$ photospheric absorption line. For the W-R star, we expect several very strong P Cygni profiles and emission lines. Crowther et al. (2000) discuss the spectrum of Sand 2, a single WO star of identical spectral type to Sand 1 but located in the LMC. Their *FUSE* spectrum, which goes from 979 to 1187 Å, shows two dominant features: the $\text{O VI } \lambda\lambda 1032, 1038$ doublet and the $\text{C III } \lambda 1175 + \text{C IV } \lambda 1168$ blend. These two line blends are clearly visible in our time-averaged spectrum of Sand 1 presented in the top panels of Figure 1 for three *FUSE* channels (SIC1A, SIC2A, and LIF2A). At lower wavelengths, we also distinguish on this plot the $\text{S VI } \lambda\lambda 933, 944$ and $\text{C III } \lambda 977$ P Cygni profiles. Sand 1 has a rather complex spectrum between ~ 1100 and 1130 Å. There are three faint emission features, the one at 1125 Å clearly from $\text{O VI } \lambda 1125$. We believe that the other two emission features, which are slightly weaker relative to $\text{O VI } \lambda 1125$ than that of

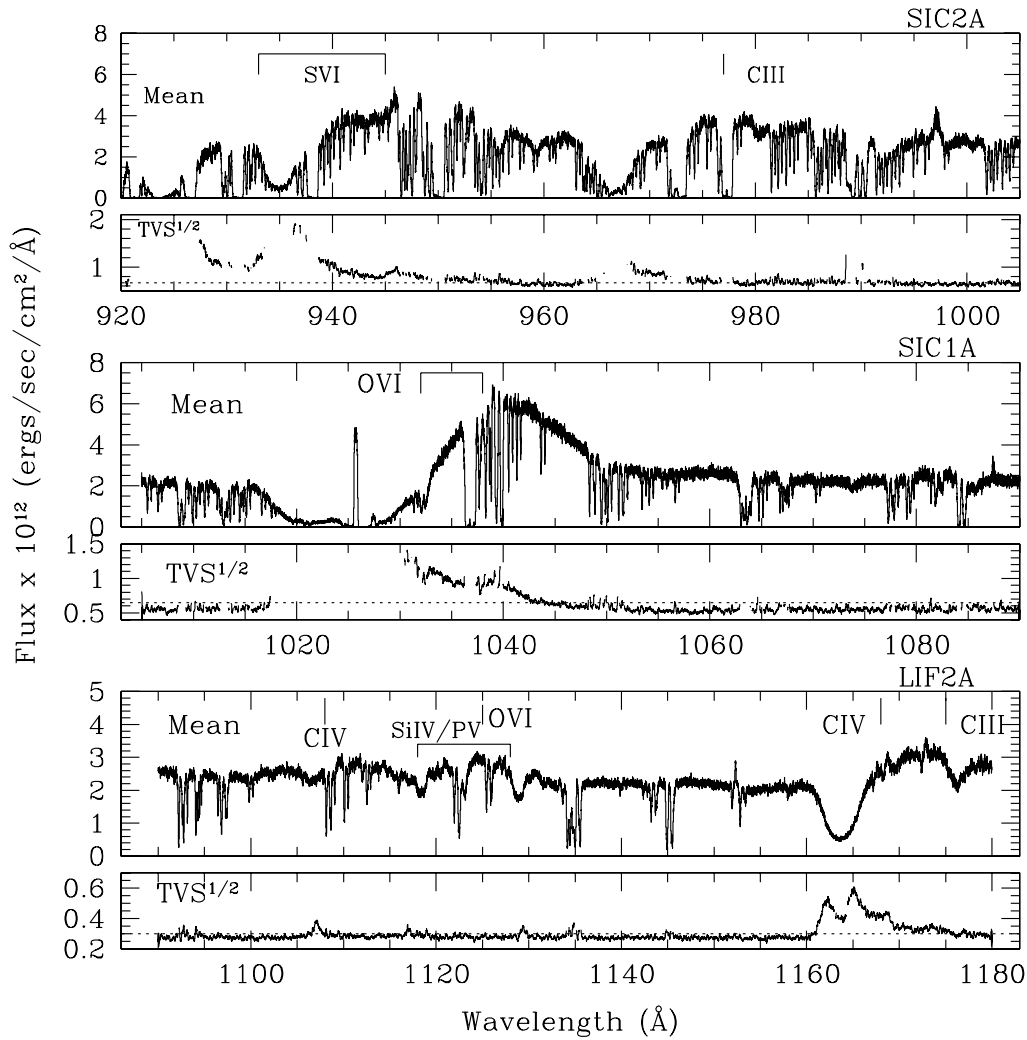


FIG. 1.—*Top panels:* Time-averaged spectrum in three channels (SIC1A, SIC2A, and LIF2A) covering the full *FUSE* wavelength region. *Bottom panels:* Square-root of the temporal variance spectrum ($\text{TVS}^{1/2}$) for our time series of spectra. The dashed line indicates the 95% confidence level for variability.

Sand 2, originate from a blend of weak P v $\lambda\lambda 1118, 1128$ P Cygni profiles and C iv $\lambda 1108$ in emission. The troughs at ~ 1106 and ~ 1117 Å are at the appropriate velocities to correspond to the P v doublet. Note that this doublet is clearly seen in the spectra of early WC stars. As the wind of the W-R star is much denser than that of the O star and its terminal velocity is much higher (4200 km s^{-1} compared to 2140 km s^{-1} ; Kingsburgh et al. 1995), the O star lines cannot be easily untangled from W-R star lines, which have nearly saturated P Cygni absorption troughs. It is very possible, however, that the completely saturated part of the O vi P Cygni absorption trough, which reaches velocities extremely close to the O star wind terminal velocity, is actually from the O star wind.

A wealth of interstellar lines is also clearly visible in Figure 1. These are mainly molecular hydrogen (H_2) lines. An excellent example of the complexity of the H_2 spectrum is presented in Figure 4 of Tumlinson et al. (2002) for the LMC star Sk $-67^\circ 166$. Absorption lines from other elements are also present (see, e.g., Richter et al. 2001).

3.2. The Variability

3.2.1. The Temporal Variance Spectrum

The bottom panels in Figure 1 show the temporal variance spectrum (TVS; Fullerton et al. 1996), which provides

a statistically rigorous means of determining which parts of the spectrum of a star show significant variability. It is given by

$$(\text{TVS})_j = \frac{\sum_{i=1}^N (w_i/\alpha_{ij})(S_{ij} - \bar{S}_j)^2}{N-1}. \quad (1)$$

In this equation, the weights of the individual spectra are $w_i = (\sigma_0/\sigma_{ic})^2$ with $\sigma_0^2 = (1/N \sum_{i=1}^N \sigma_{ic}^{-2})^{-1}$, where σ_{ic} is the noise in the continuum (estimated by fitting a linear function to selected regions of continuum for each channel; see below). The wavelength correction factors are given by $\alpha_{ij} = (\sigma_{ij}/\sigma_{ic})^2$, and \bar{S}_j is the weighted mean spectrum. For the value of the noise of pixel j in spectrum i , σ_{ij} , we have adopted the value provided by the *FUSE* project.

Shown in the figure is $\text{TVS}^{1/2}$, which scales linearly with the size of the spectral deviations. It is clear from this figure that our data show variability mainly in the strongest spectral lines and especially in the P Cygni absorption edges. Note that the saturated P Cygni absorption troughs and interstellar lines have been avoided, since no significant information can be obtained for them. The dotted line is the $[\sigma_0^2 \chi_{N-1}^2(95\%)]^{1/2}$ value, which indicates a 95% significance level for the variability. The level of variability is highest in the regions covering the

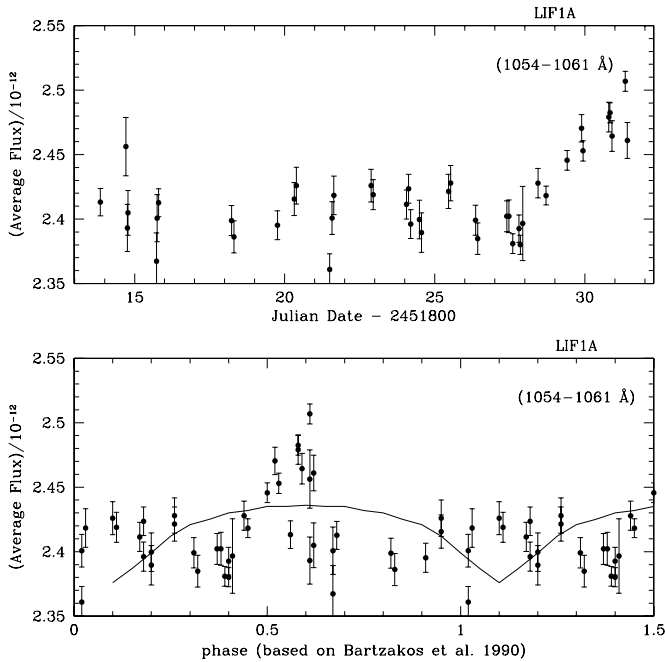


FIG. 2.—Average continuum flux in LIF1A for the 1054–1061 Å wavelength region plotted as a function of Heliocentric Julian Dates (*top*) and as a function of the Bartzakos et al. (2001) phases (*bottom*). The curve in the bottom panel is a model light curve calculated with our shock-cone emission plus atmospheric eclipse SEI code (see § 4.3).

unsaturated parts of the absorption components, although the variability is significant over most of the extent of all the main P Cygni profiles present in our spectra. The fact that the variability that we have detected through profile comparison and gray-scale plots (see § 3.2.2) in the red part of the emission components does not appear to be significant in the TVS analysis most likely indicates that the error values, σ_{ij} , provided by the CALFUSE version 2.3.0 pipeline are still slightly too high.

We caution that in the above analysis we have scaled the spectra to a common continuum level (that of the first spectrum A12302-63) using appropriate line-free wavelength regions (960–962 Å for SIC2A, 1075–1076.5 Å for SIC1A, and 1146.5–1149 Å for LIF2A). This, of course, effectively removes any variations in the continuum. Therefore, the lack of significant TVS variability detection between the main wind lines only reflects the adopted analysis method. The reason that we have adopted this technique is that the average flux value in selected continuum regions for the various channels did not appear completely stable for the detector segments presented here (SIC1A, SIC2A, and LIF2A). Although the continuum flux values are stable in general, there are occasional increases reaching up to 30%. These increases are uncorrelated in the three channels, indicating that they do not originate in Sand 1. Remembering that our target is located in the SMC, we speculate that these increases are very likely caused by neighboring stars occasionally coming into the (relatively large) slit due to grating or mirror misalignments.

One channel that should not present such problems is LIF1A. Indeed, this detector segment is the least likely to be affected by mirror and grating alignments since it is closely linked to the FES guiding camera. In the top panel of Figure 2, we plot the average LIF1A flux in a wavelength region apparently devoid of spectral lines (1054–1061 Å) as a function of time for our data set. For each spectrum, the error bars have been estimated

using the CALFUSE pipeline errors on the flux at each wavelength, σ_{ij} , as follows:

$$\sigma_j = \frac{\sqrt{\sum_{i=1}^N \sigma_{ij}^2}}{N},$$

where N is the number of flux points to be averaged (the *FUSE* LIF1A pixel has a width of 0.067 Å).

In Figure 2 we also present the different exposures of a given observation separately, to show the scatter. The average continuum flux remained relatively stable during the first 15 days but then quickly rose during the last 3 days. Although we do not have two different orbital cycles to check whether this change is strictly periodic, it is interesting to look at the variations as a function of orbital phase. This is plotted in the bottom panel of Figure 2. The rise is centered on phase 0.55 and has a width of 0.2 in phase. This light curve can be compared with the optical light curve presented, for example, by Moffat et al. (1985) essentially repeated and accompanied by a different, noisier one in Seggewiss et al. (1991). The optical curve has quite a different appearance, showing a brightening near phase 0.0 with a width of 0.7 in phase and an amplitude ~ 2 times smaller. Note that this type of optical light curve is unusual among W-R+O binaries. More often, a decrease due to the atmospheric eclipse of the O star continuum by electrons in the W-R wind is observed at that phase (Lamontagne et al. 1996). Because of their distinct behavior, it is therefore unlikely that the optical and UV photometric variations originate through the same physical phenomenon. If we do, however, force both maxima to coincide, we obtain a time difference between them of 6843.75 days. If we use this to recalculate the orbital period, we obtain $P = 16.65 \pm 0.03$ days, where we have estimated a 0.5 day error in the time difference between both peaks. This would lead to a phase difference of $\Delta\phi = -0.35$ compared to the phases obtained using the Bartzakos et al. (2001) period. However, this is unlikely to represent an improvement on the previous estimations of the period of Sand 1, because the number of data sets used is small and we cannot be sure that the UV and optical light maxima can be ascribed to the same physical phenomenon.

3.2.2. The Nature of the Spectral Variability

In order to determine whether the variability that we have detected is binary-related, we have organized our time-series of spectra as a function of orbital phase. The most recent determination of the orbital parameters of Sand 1 is by Bartzakos et al. (2001), who give $P = 16.633 \pm 0.009$ days and $E_0 = \text{HJD } 2,446,032.9 \pm 0.1$ (time of the W-R inferior conjunction; circular orbit solution). The orbital phases of individual spectra are listed in Table 1. In view of the error on the period and the time elapsed since this zero point, we cannot, however, use the orbital-phase zero point with any confidence to locate the relative positions of the stars. Instead, we have used an O star absorption blend present in our *FUSE* spectrum, Si IV/P v $\lambda 1128.0$, to recalculate the binary period. We have measured the radial velocities of this line by fitting a Gaussian profile and plot the results in Figure 3 as a function of the phase calculated with the Bartzakos et al. (2001) ephemeris. Although this absorption line is superposed on the O v $\lambda 1125$ emission line, it does yield quite a clean orbital curve. This is because this emission line does not present any significant variability above the noise level of our spectra.

The solid line is a fit of a circular orbit, and the dashed line is for an elliptical orbit. The resulting parameters can be found in

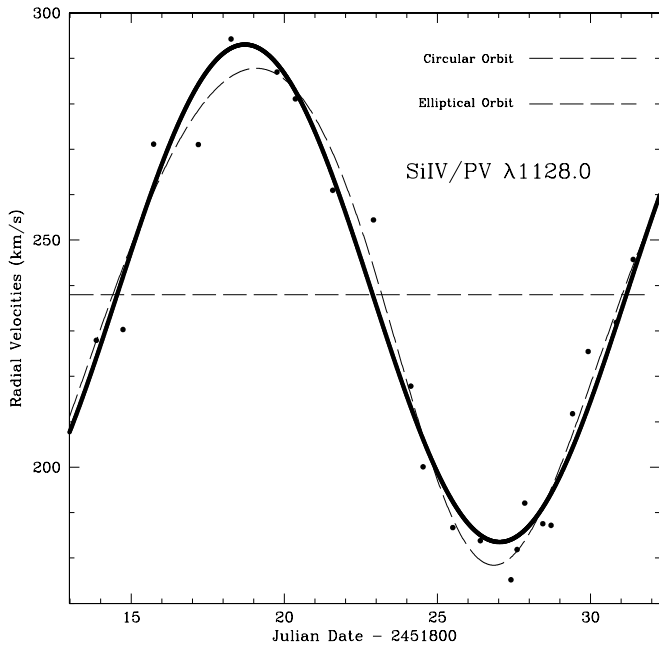


FIG. 3.—Radial velocity of the O star Si IV/P v $\lambda 1128.0$ absorption line as a function of the orbital phase calculated with the Bartzakos et al. (2001) ephemeris. We show fits to circular (solid line) and elliptical (dashed line) orbits.

Table 2. Here we adopt the circular orbit solution since the elliptical orbit is not a major improvement of the fit. Using the observed time of passage through the gamma velocity, we obtain an updated period of $P = 16.638$ days, well within the error margin given by Bartzakos et al. (2001). It is worth noting that no obvious profile shape changes of the Si IV/P v $\lambda 1128.0$ absorption feature are detected in our data.

To illustrate the detected variability, we present in Figure 4 the 21 individual spectra (colored lines) in the wavelength region spanning the O VI $\lambda\lambda 1032, 1038$ doublet as a function of orbital phase calculated with our new estimate of the period (and using the Bartzakos et al. 2001 zero point in time for a circular orbit) indicated on the right-hand side of the plots (one of the spectra, obtained at phase 0.66, was corrupted in this channel and therefore cannot be shown in this plot). Successive spectra, which have been smoothed with a box-car average of 15 pixels, are displaced in ordinate in order of (but not proportional to) their orbital phase. The left-hand panel displays data from phases 0.0–0.5, while the right-hand side of the plot shows our data for phases 0.5–1.0. Close inspection of the variability and comparison with other well-known colliding-wind systems (e.g., St-Louis et al. 1993) led us to the conclusion that the changes were caused by the combined effect of atmospheric eclipses and excess emission from a wind-wind collision shock cone. Therefore, we have constructed a “reference” spectrum (shown as dark lines in Fig. 3) by taking into account the following considerations:

1. In view of the high velocity value reached by the winds in this system compared to the orbital speeds, Coriolis effects on the shock-cone emission will be small. Indeed, the shock-cone angle deflection is roughly given by $\delta\phi \approx \arctan[v_{\text{orbital}}(\text{O} + \text{W-R})/v_{\text{wind}}(\text{W-R})]$, where $v_{\text{orbital}}(\text{O} + \text{W-R}) = (K_{\text{O}} + K_{\text{W-R}})/\sin i$ is the sum of the orbital velocities of the O and W-R stars ($K_{\text{O}} = 55 \text{ km s}^{-1}$, this paper; and $K_{\text{W-R}} = 157 \text{ km s}^{-1}$, Bartzakos et al. 2001) and $v_{\text{wind}}(\text{W-R})$ is the terminal velocity of the W-R wind [$v_{\infty}(\text{W-R}) = 4200 \text{ km s}^{-1}$, from UV P Cygni pro-

TABLE 2
ORBITAL FITS TO Si IV/P v $\lambda 1128.0$ RADIAL VELOCITIES

Parameter	Fitted Value
Circular Orbit	
P (days).....	16.633 (fixed)
E_0 (HJD).....	2,446,032.9
K (km s^{-1}).....	54.8
V_{γ} (km s^{-1}).....	238.29 ± 0.23
$\sigma(o - c)$ (km s^{-1}).....	7.44
Elliptical Orbit	
P (days).....	16.633 (fixed)
K (km s^{-1}).....	54.7 ± 1.6
e	0.10 ± 0.03
ω (deg).....	149.4 ± 15.3
T_0 (HJD).....	$2,451,825.69 \pm 0.69$
V_{γ} (km s^{-1}).....	237.97 ± 1.15
$\sigma(o - c)$ (km s^{-1}).....	4.42

files by Kingsburgh et al. 1995]. Therefore, using $i = 40^\circ$ (see a discussion of why this value was adopted in § 4.2), we obtain $\delta\phi \approx \arctan[(157 + 55)/4200 \sin 40^\circ] \approx \arctan(0.079) \approx 4.5^\circ$, which can essentially be neglected. Excess emission from a colliding-wind shock cone therefore should produce a relatively symmetric pattern with respect to conjunction.

2. When the shock cone is pointing toward us (O star \sim at inferior conjunction, phase 0.5), the excess emission is shifted to the blue, while when the shock cone is pointing away from us (O star at superior conjunction), it is shifted to the red.

3. From the geometry of such binaries, it is clear that the atmospheric eclipse has a maximum width when the O star is behind the W-R star and decreases toward the blue as the O star comes in front of the W-R star. If the O star orbits completely outside the line formation zone, then the additional absorption component introduced by the atmospheric eclipse will be symmetrical with respect to the gamma velocity. If part of the W-R line formation zone is outside the O star orbit, some absorption will be missing on the red part of the profile.

From the above points, we deduce that the red side of the profile is only affected when the O star is *behind* the W-R star and the atmospheric eclipse occurs at these wavelengths. Therefore we have used spectra on either side of the symmetry point (when the O star is in front) to form the red side of the reference profile (in this case, wavelengths longer than 1038 \AA). For these phases, the excess emission is shifted to the blue and there is no atmospheric eclipse in the red parts of the spectral lines, and therefore the red part of the profiles should be unaffected. Inspection of the data led us to determine that the point of symmetry is at $\phi \sim 0.5$ as expected. We have therefore used spectra with numbers 63, 64, 65, 77, 78, and 79, which are close to phase ~ 0.5 (see Table 1), to determine the red part of the reference spectrum. Note that the new period ($P = 16.638$ days) implies a phase shift relative to the Bartzakos et al. (2001) phases of $\delta\phi = -0.1$. We will adopt this new period along with E_0 from Bartzakos et al. (and corresponding orbital phases) for the remainder of this paper.

Deciding what to use as a reference spectrum for the blue side is more complicated. Indeed, when the O star is in front, the excess emission from the shock cone is shifted to the blue, and when the O star is in back, although the excess emission is on

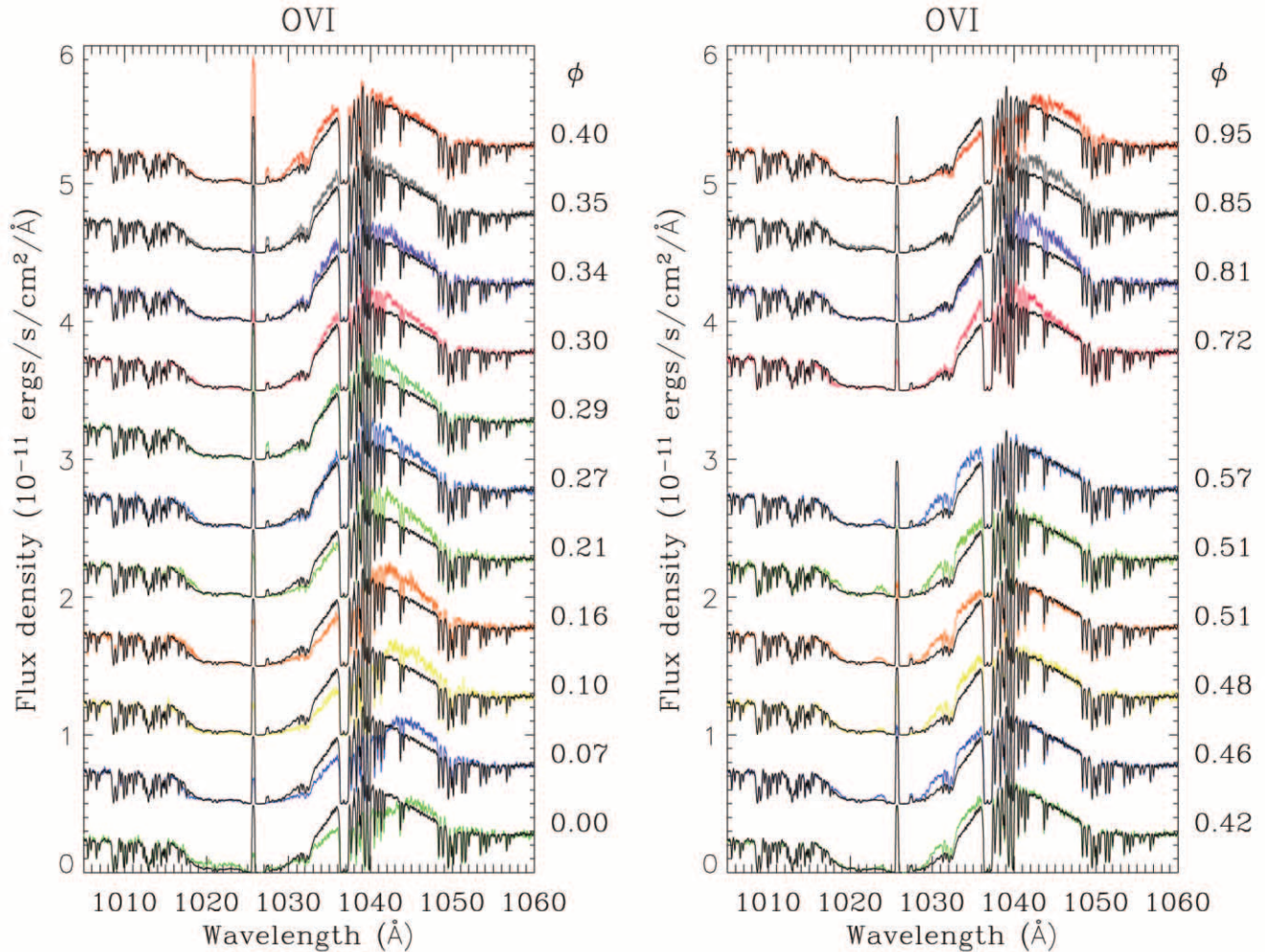


FIG. 4.—Stack of SIC1A spectra showing the variability in the O VI $\lambda\lambda 1032, 1038$ doublet. The dark line is our reference spectrum (see text), and the phase (using the current improved ephemeris) of each colored line is indicated on the right-hand side of the plots.

the red side, the atmospheric eclipse is strong, particularly in the blue. Note that when the O star is in front, the blue side of the profile could also be affected by atmospheric eclipse effects if the line formation zone is exterior to the orbit. Our best strategy is therefore to use three spectra right after first quadrature (at $\phi = 0.25$) and three right after the second quadrature (centered at $\phi = 0.75$); the small excess emission in the blue from the spectra right after first quadrature then roughly cancels out with the small absorption from the eclipse occurring after second quadrature, thereby providing the closest thing one can probably get to an unperturbed blue-side spectrum. Visual inspection of individual spectra at these phases confirms that there is no large-scale variability on the blue side of the profile at these phases. We have therefore used spectra with numbers 68, 69, 75, 76, 81, and 4 (see Table 1) to determine the blue part of the reference spectrum. Note that as the reference spectrum for each profile is constructed from averages of two different sets of spectra, there could be a slight flux inconsistency at the central interface wavelength (zero velocity). This must be taken into account when interpreting the differences between individual spectra and the reference spectrum. In summary, our red reference spectrum is free of both atmospheric eclipses and wind-wind shock emission, while our blue reference spectrum is also relatively free of these effects, but this time because the two

effects roughly cancel out, one being in emission and the other in absorption.

We have also revisited the Bartzakos et al. (2001) optical spectroscopic data to compare with our line profile variability. In Figure 5 we have reproduced their Figure 12, showing the C IV $\lambda 5808$ excess emission as a function of phase (calculated with their own ephemeris). Although weak, it is possible to trace the emission feature as it moves around in phase (note that no atmospheric eclipse is detected in this line).

In order to trace the position of the excess emission profile in velocity as a function of phase, we have measured the FWHM of the profiles as traced by their blue and red edges. The measured intervals are shown by a thick black line in Figure 5 for each profile. In Figure 6 we plot the velocity of the blue and red edges of the profiles, as well as the average of these two velocities, as a function of their orbital phase (the solid curves are discussed below). There is a clear phase shift (~ 0.13) between the C IV $\lambda 5808$ excess emission and the O star position on its orbit. As the ephemeris used in this plot was determined from their own optical data, we conclude that this phase shift is real.

In fact, this shift between the optical radial velocities and the excess emission in the C IV $\lambda 5808$ line can perhaps be understood if one considers the geometry of the shock cone and how the emission is actually formed. At the bow shock head, the gas

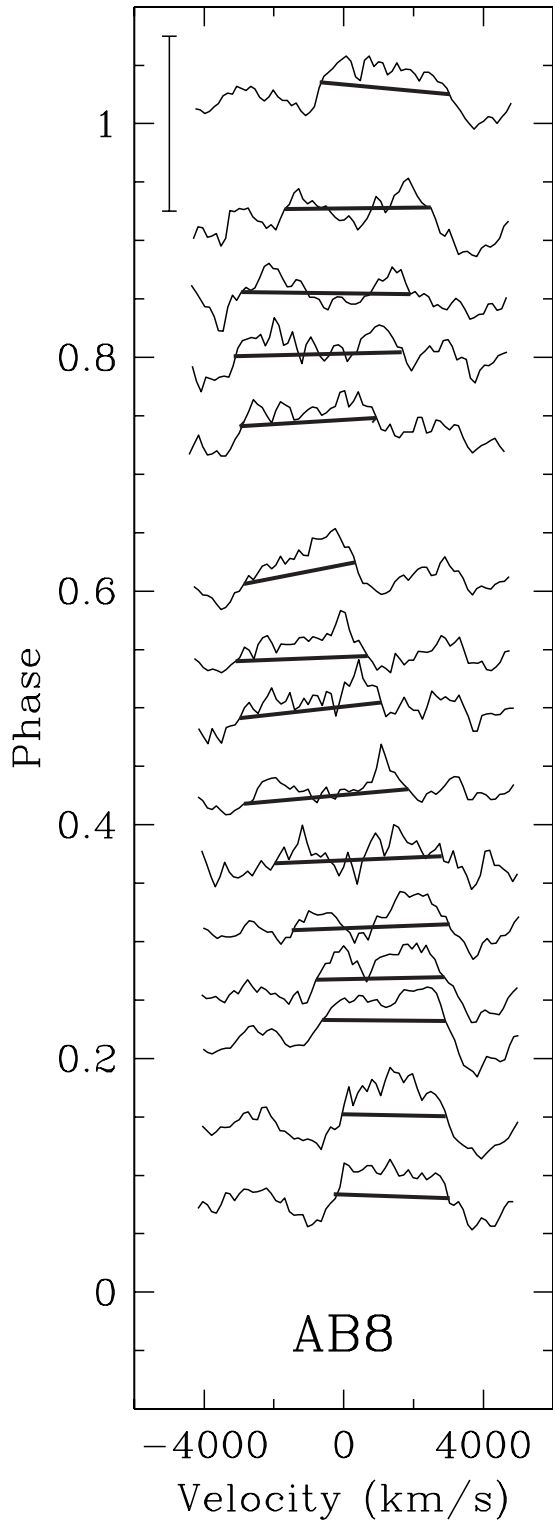


FIG. 5.—Excess-emission profiles from the shock cone in Sand 1 (=AB8) for the C IV $\lambda 5808$ line, taken from Fig. 12 of Bartzakos et al. (2001). The height of the vertical bar shows 50% of the continuum intensity. The phase of each spectrum is indicated on the left-hand side of the plot. We have added thick, dark lines to indicate the FWHM measurements made for each profile. The lines are often slightly slanted, due to noise and systematic rectification errors.

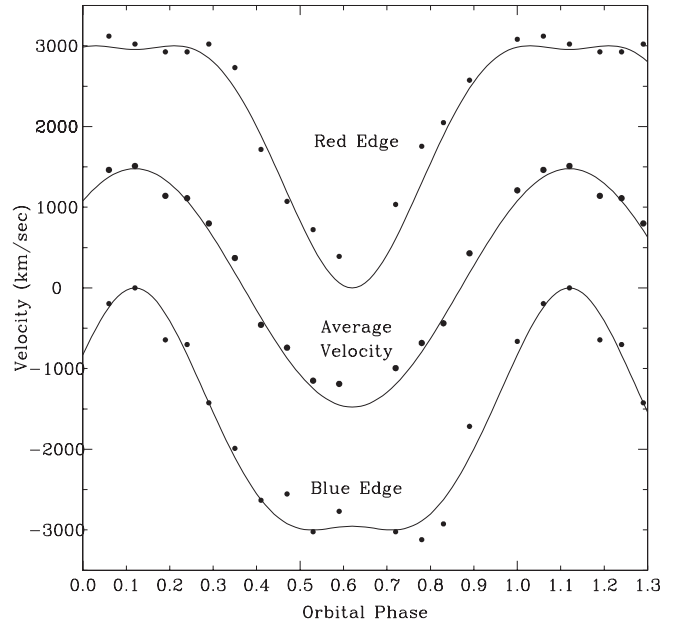


FIG. 6.—Measurements of the shock-cone emission of Sand 1 (=AB8) for the C IV $\lambda 5808$ line from Bartzakos et al. (2001). The measured interval bounded by the blue and red edges plotted here are indicated for each individual profile in Fig. 5. The curves refer to eqs. (2), (3), and (8). Note the sinusoidal symmetry of the average radial velocity curve compared to the distorted, antisymmetric nature of the line edges.

is far too hot to emit at optical and UV wavelengths. As the gas flows along the shock away from the star, it cools, and once it reaches the appropriate temperatures it will emit in spectral lines. The shock cone is traced by gas particles, which are actually moving nearly in a straight line away from the system. Their trajectory only appears curved because of the orbital motion of the region in which they originate, i.e., the bow shock head. It takes time for the particles that constitute the shocked gas to reach a location on the shock cone where temperatures render it possible for them to recombine into ions that emit in the UV and even more in the optical. In the meantime, the O star has progressed on its orbit around the W-R star (strictly speaking, around the center of mass). If the material has to travel far along the shock cone before it can emit in spectral lines, there could easily be a phase shift between radial velocities and excess emission. The data tell us that it is only when the companion is at phase 0.63 (O star coming out of inferior conjunction) that the shocked gas reaches temperatures appropriate for C IV $\lambda 5808$ excess emission in Sand 1. This delay effect is also what creates the resolved Archimedean dust spirals (called pinwheel nebulae) so clearly observed for WR 104 and WR 98A by Tuthill et al. (1999) and Monnier et al. (1999), respectively. In a sense, what we are observing here is the birth of a potential pinwheel nebula. However, in order to produce such a phase shift, the material would have to travel for $\sim 0.13 \times 16.633$ days ~ 2 days. For velocities along the shock cone between 2000 and 4000 km s⁻¹, this corresponds to ~ 500 –1000 R_{\odot} . It is theoretically unclear whether the densities at these distances along the shock cone are high enough to produce the observed fluxes.

As for the variability, we will begin with a qualitative description of what we observe. One can clearly see in Figure 4 the excess emission in the red near phase 0 (W-R in front) and the excess emission in the blue near phase 0.5 that characterizes colliding-wind emission. Also visible at phase 0 (O star in back)

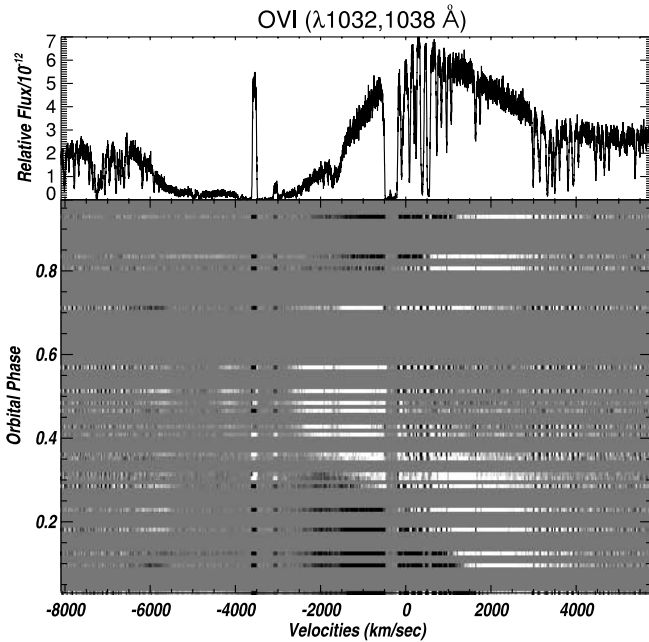


FIG. 7.—Gray-scale plot of differences between individual spectra and the reference spectrum (*top*) described in the text for O VI $\lambda\lambda 1032, 1038$, illustrating the spectral-line variability.

is an excess of absorption on the blue side of the emission profile, which becomes narrower with increasing phase as the O star moves from the backside to the frontside of the W-R star; this is expected from selective wind eclipses. There is, of course, interference between these two effects, which prevents us from seeing the full extent of the atmospheric-eclipse absorption-profile on the red side and occasionally the full width of the shock-cone excess emission. Furthermore, the saturation of the P Cygni absorption also hides part of the atmospheric eclipse profile in the blue.

In order to show the variability in a more compact fashion, we present in Figures 7–10 gray-scale plots of the differences between each individual spectrum and the reference spectrum mentioned above for the major lines present in the spectrum. In the bottom panels, each differenced profile is shown as an intensity profile and displayed in velocity space to facilitate comparison with other lines, and is placed vertically according to its orbital phase (indicated by the y -axis labels). In the top panels, we present the reference spectrum that was used to generate the difference spectra.

The clearest case is for O VI $\lambda\lambda 1032, 1038$, which is shown in Figure 7. The excess emission from the shock cone is clearly seen as a bright S-shaped feature moving from red to blue from phase 0.0 to 0.5 and back again from phase 0.5 to 0.0. The actual excess emission varies in intensity, reaching $\sim 25\%$ of the maximum O VI emission flux (see also Fig. 4). The extreme edges of the excess emission reach a maximum velocity of $\sim \pm 2500$ km s $^{-1}$. The atmospheric eclipse is seen as a dark triangle located mainly to the blue of line center starting very wide near phase 0.0 and disappearing near phase 0.4. From phase ~ 0.7 to phase 1.0 the reverse happens; the dark profile starts narrow and widens with increasing phase. This is as expected from the geometry of binary systems. In fact, the absorption profile from the atmospheric eclipse should be even wider, but the saturated black trough prevents us from seeing its full extent in the blue, and it is partially filled in by the excess emission from the shock cone in the red. In principle, near

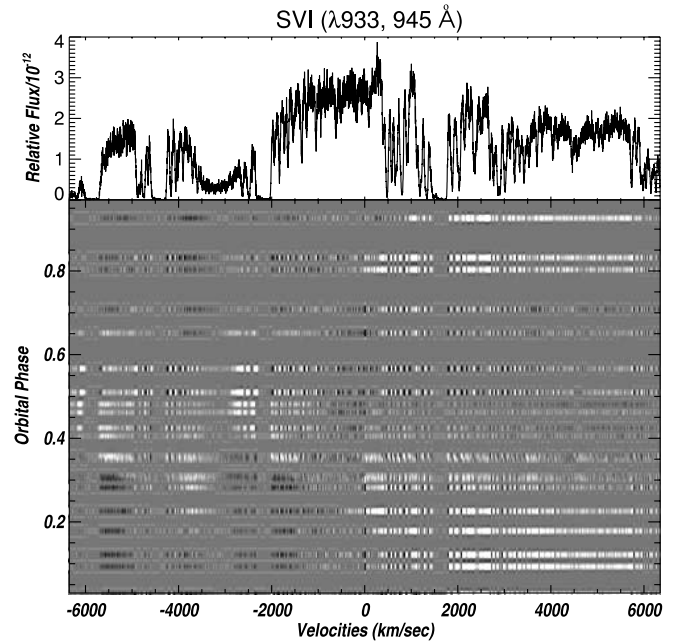


FIG. 8.—Same as Fig. 7, but for S VI $\lambda\lambda 933, 945$.

$\phi \sim 0.0$, one could detect some strengthening of the absorption at high negative velocities, $v \sim v_\infty$, where the profile slants back up. The fact that we do not see any absorption at these velocities strongly suggests that the orbital inclination is rather low. One can clearly see in these gray-scale plots, as expected, that the movement of the excess emission from the shock cone (the bright S-shaped feature) is symmetric with respect to phase 0.5 and the atmospheric absorption component appears to be symmetric around phase 0.0.

Figure 8 shows the corresponding gray-scale image for the S VI $\lambda\lambda 933, 945$ doublet. This line pair presents a similar pattern of variability as O VI $\lambda\lambda 1032, 1038$, except that the S VI doublet separation is big enough that we can clearly see the two excess

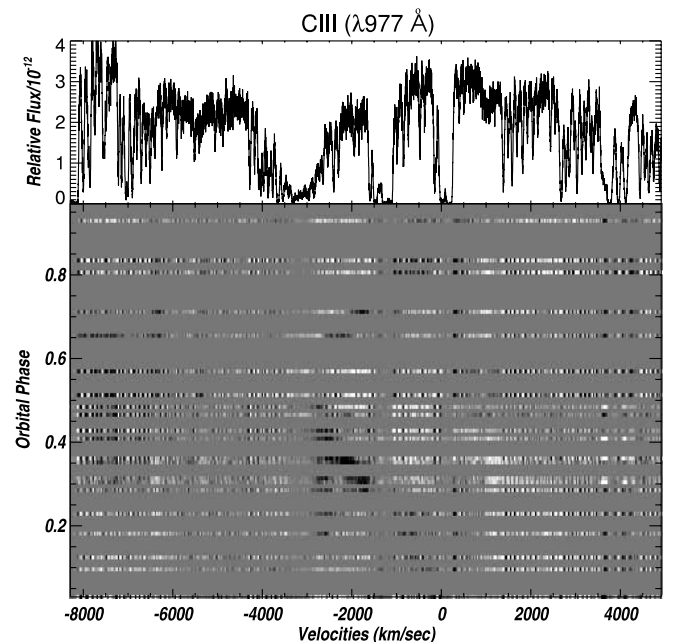


FIG. 9.—Same as Fig. 7, but for C III $\lambda 977$.

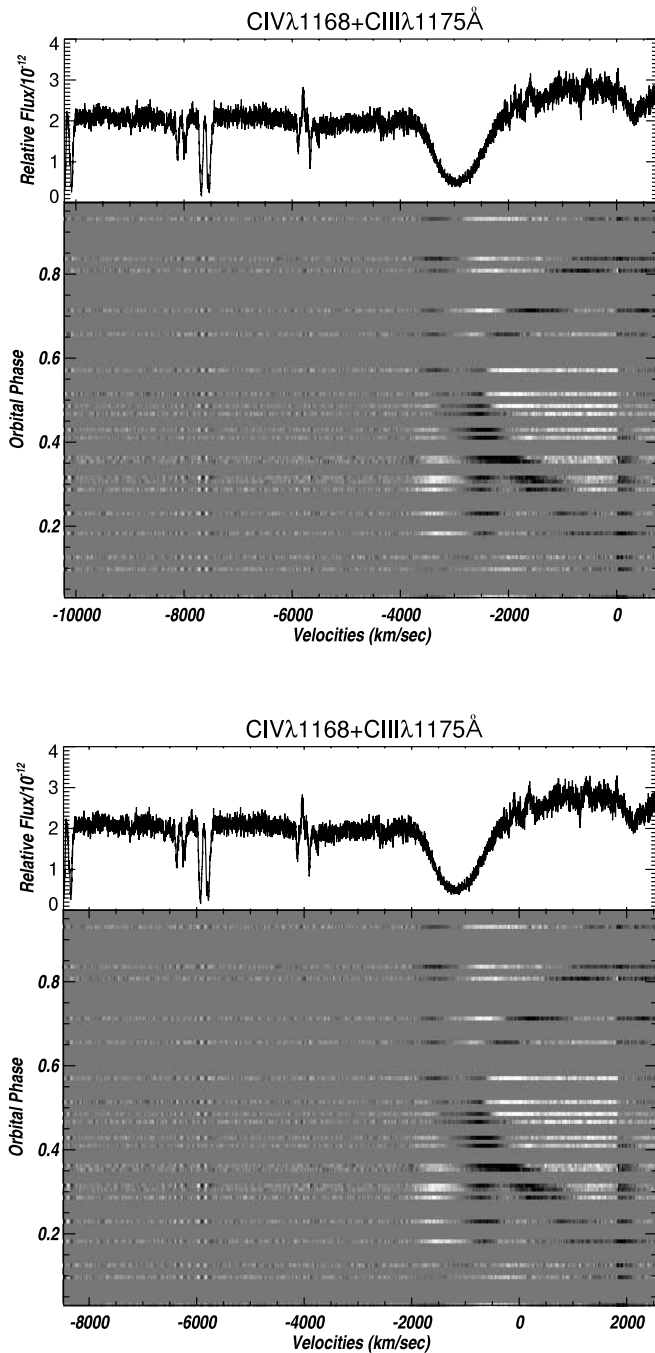


FIG. 10.—Same as Fig. 7, but for C IV $\lambda 1168 + \text{C III } \lambda 1175$. *Top*: Velocities calculated with $\lambda_0 = 1175 \text{ \AA}$. *Bottom*: Velocities calculated with $\lambda_0 = 1168 \text{ \AA}$.

emission profiles moving in phase. The velocity range, covered by this feature is the same as for O VI $\lambda\lambda 1032, 1038$. The atmospheric eclipse is also seen for both components of the doublet, covering a similar velocity range. Once again, saturation and confusion effects prevent us from seeing its full extent.

For the C III $\lambda 977$ line the intensity variations, shown in Figure 9, have a much smaller amplitude and therefore the contrast is much lower in the gray-scale plot. Nevertheless, the S-shaped pattern can be distinguished with a similar velocity extent as for the O VI and S VI doublets. The dark triangles generated by the atmospheric eclipse are also present but are partially filled in by excess emission in the ~ -1500 to -3000 km s^{-1} velocity range between phases 0.9–1.2 and 0.7–0.9. It is unclear where this

emission originates, but it is perhaps linked with the still unexplained excess emission in the optical continuum, which occurs at very similar phases.

The variability pattern for the C IV $\lambda 1168$ and C III $\lambda 1175$ blend presented in Figure 10 is even more complicated. First, the *FUSE* wavelength range does not cover the full extent of the line from this very fast W-R wind. Indeed, the C IV $\lambda 1168$ line is missing in the velocity range above $+2000 \text{ km s}^{-1}$ while the C III $\lambda 1175$ line is only visible up to $\sim +500 \text{ km s}^{-1}$. We have used a similar velocity range as for the other gray-scale plots to facilitate comparison. This is useful to compare the variable parts of the spectrum with those devoid of lines (i.e., between $-10,000$ and -4500 km s^{-1} in Fig. 10).

When plotted on the C III $\lambda 1175$ velocity scale (*top panel*), one can clearly see part of the S-shaped excess emission at phases 0.3 to 0.6 and the dark triangles generated by the atmospheric eclipses. Once again, the latter is partially filled in by excess emission in the ~ -1500 to -3000 km s^{-1} velocity range, as seen for the C III $\lambda 977$ line. However, because the C III $\lambda 1175$ absorption trough is not completely saturated, we can see the dark eclipse triangle extending to higher velocities ($\sim -3500 \text{ km s}^{-1}$). We therefore conclude that these structures result from variations in the number of C III ions rather than C IV ions.

The only feature that remains unaccounted for is some excess emission appearing at -3000 to -4000 km s^{-1} near phase 0.3. However, when plotted on the C IV $\lambda 1168$ velocity range, it appears that this feature could be part of the an S-shaped structure from C IV ions. The dark triangle from the eclipse in C III $\lambda 1175$ ions hides the rest of the feature. There is clearly no atmospheric eclipse in C IV $\lambda 1168$, as this would produce a dark triangle reaching high negative velocities, since there are no saturation or blending effects. Indeed, the spectrum to the blue of the C IV $\lambda 1168 + \text{C III } \lambda 1175$ blend seems to be mainly continuum.

4. AN ANALYSIS OF THE SPECTRAL-LINE VARIABILITY

4.1. What Can Be Learned from the Spectral-Line Variability

The variations described in the previous section reveal several interesting phenomena taking place in this binary system. First, the TVS analysis indicates that *all* the major lines in the spectrum show variability. Examination of the pattern of variability has allowed us to deduce that the changes are caused by atmospheric eclipse of the O star continuum by the wind of the W-R star and by excess emission from a shock cone generated from the wind-wind collision.

A simple geometrical model developed by Lührs (1997) can be applied to spectroscopic observations of lines that are little sensitive to atmospheric eclipses, to obtain a rough estimate of the parameters describing the bow shock. This will be done in § 4.2. For lines that are sensitive to both atmospheric eclipses and wind-wind collision effects, one has to fit the line-profile variability with a model that simultaneously includes both effects. Such a model is discussed in § 4.3 for the O VI $\lambda\lambda 1032, 1038$ and S VI $\lambda\lambda 933, 945$ doublets. These ions have significantly different ionization potentials (113.9 eV compared to 72.7 eV).

One interesting result is that the S-shaped feature from the shock cone is similar for all spectral lines. Indeed we would have expected that as lines are formed closer and closer to the hot bow shock cone-shaped “rounded” head (O VI compared to C III for example), the deduced opening angle would become larger. This is *not* what is observed. We conclude that the cooling must be sufficiently slow at first that even lines such

as the O VI $\lambda\lambda 1032, 1038$ doublet are formed in essentially the linear part or at least very close upstream of the cone as those of C III. This will be examined in more detail in § 4.4.

4.2. An Analytical Model

Lührs (1997) presented a purely geometrical model of line emission from a shock cone produced by wind-wind collision in a massive binary in a circular orbit. This model allows one to make a rough estimate of the parameters of the shock cone where the lines are formed, namely, the half-opening angle, θ , and the streaming velocity of the gas along the shock cone, v_{str} , which is assumed constant. This analysis also provides an estimate of the orbital inclination, i . In this section we will apply this model to the variations observed for Sand 1 in the optical C IV $\lambda 5808$ line, which were originally presented (without applying the Lührs 1997 model) by Bartzakos et al. (2001). Note that the C III $\lambda 5696$ line often used to trace colliding winds in the optical for W-R+O binaries is completely absent from the WO star wind and from the wind-wind collision zone. This recombination line is more suited for this analysis because the variations in this transition are solely from shock emission, with no detectable atmospheric eclipse effects.

We base our analysis on the measurements of the velocities of the blue and red edges of the shock emission profiles (see Fig. 6). According to the Lührs model, the emission from the shock cone presents itself mainly as two peaks moving in phase but at different rates. The equations of Lührs (1997) describe the central velocities for each of the two peaks. Since we do not have access to these peak values, mostly due to the low amplitude of the variations and to a relatively large noise level, we measure instead the more visible blue and red *edges* of the overall excess profile at half maximum ($v_{\text{red}}, v_{\text{blue}}$). Assuming that each of the two peaks have a constant width (probably not strictly true), our measurements will only differ from the equations of Lührs (1997) by a constant ($C_1 > 0$) that equals the half-width of the excess emission peaks at half maximum. Since in this section we only wish to deduce approximate values, this assumption is sufficient for our purpose. With phases from the Bartzakos et al. (2001) ephemeris, the equations describing the velocities of the blue and red edges of the profile are then given by

$$v_{\text{red}} = C_1 + v_{\text{str}} \cos \theta \sin i \cos \phi^* + v_{\text{str}} \sin \theta \sqrt{1 - \sin^2 i \cos^2 \phi^*}, \quad (2)$$

$$v_{\text{blue}} = -C_1 + v_{\text{str}} \cos \theta \sin i \cos \phi^* - v_{\text{str}} \sin \theta \sqrt{1 - \sin^2 i \cos^2 \phi^*}, \quad (3)$$

where ϕ^* is the corrected orbital phase, $\phi^* = \phi + \delta\phi$. This $\delta\phi$ is caused by the combined effects of the Coriolis twist, which in our case is negligible, and by the effect mentioned in § 3.2.2 related to the delay in the emission of the optical line flux as the material flows along the shock cone.

From these two equations, we deduce an expression for the FWHM of the shock emission profile as a function of the corrected orbital phase:

$$\text{FWHM} = v_{\text{red}} - v_{\text{blue}} = 2C_1 + 2v_{\text{str}} \sin \theta \sqrt{1 - \sin^2 i \cos^2 \phi^*}. \quad (4)$$

The FWHM describes a double-wave curve per orbital cycle and has the following maximum and minimum values with phase:

$$\begin{aligned} \text{FWHM}_{\text{max}} &= 2C_1 + 2v_{\text{str}} \sin \theta, & (5) \\ \text{FWHM}_{\text{min}} &= 2C_1 + 2v_{\text{str}} \sin \theta \cos i. & (6) \end{aligned}$$

From the ratio of these two values, the orbital inclination can be deduced. From the profiles of Figure 5, we measure $\text{FWHM}_{\text{max}} = 4655 \text{ km s}^{-1}$ and $\text{FWHM}_{\text{min}} = 3175 \text{ km s}^{-1}$. We therefore obtain

$$\cos i = \frac{(\text{FWHM}_{\text{min}} - 2C_1)}{(\text{FWHM}_{\text{max}} - 2C_1)} = \frac{3175 \text{ km s}^{-1} - 2C_1}{4655 \text{ km s}^{-1} - 2C_1}. \quad (7)$$

In our case, we cannot actually measure C_1 , as we do not resolve the individual components. For C_1 going from 0 to 750 km s^{-1} , which corresponds to a very rough estimate from Figure 5 (from the spectra at phases 0.3 and 0.9, for example), we find $i \approx 47^\circ - 58^\circ$.

From the radial-velocity curve and assuming a mass of $50 M_{\odot}$ for the O4 companion, Moffat et al. (1985) estimate the inclination angle to be $i \approx 30^\circ$. These authors also point out that in order to explain the light curve, the orbital inclination should be well below $\sim 60^\circ$. The values at the lower end of our range are therefore more compatible with their estimate. Also, in § 4.5 we present line-profile fits from which we deduce $i = 35^\circ \pm 5^\circ$. In view of the fact that our estimate of the inclination from the optical C IV profiles is extremely uncertain, mainly because of the high level of noise in the data, we adopt a value of $i = 40^\circ \pm 10^\circ$.

From equations (2) and (3), we can also define a quantity, which we will call the mean radial velocity of the shock emission profile, RV_{ex} , as

$$\text{RV}_{\text{ex}} = \frac{v_{\text{red}} + v_{\text{blue}}}{2} = +v_{\text{str}} \cos \theta \sin i \cos \phi^* = +A \cos \phi^*, \quad (8)$$

with $A = v_{\text{str}} \cos \theta \sin i$.

From equations (5), (6), and (8), we deduce the half-opening angle of the shock cone:

$$\begin{aligned} \frac{(\text{FWHM}_{\text{max}} - \text{FWHM}_{\text{min}})}{A} &= \frac{2v_{\text{str}} \sin \theta (1 - i)}{v_{\text{str}} \cos \theta \sin i} \\ \implies \tan t\theta &= \frac{(\text{FWHM}_{\text{max}} - \text{FWHM}_{\text{min}}) \sin i}{2A(1 - \cos i)}. \end{aligned} \quad (9)$$

From Figure 6, the fit gives $A = 1375 \text{ km s}^{-1}$. For $i = 40^\circ$ this yields

$$\theta = 56^\circ.$$

We can insert this value into the equation of Usov (1992),

$$\theta(\text{deg}) = 120 \left(1 - \frac{\eta^{2/5}}{4} \right) \eta^{1/3},$$

to estimate, η , the momentum ratio of the two winds. The half-opening angle of the cone determined here yields $\eta = 0.15$. We already have a good estimate of the terminal velocities of the winds of the two components of the binary from Kingsburgh et al. (1995): $v_{\infty}(\text{W-R}) = 4200 \text{ km s}^{-1}$, $v_{\infty}(\text{O}) = 2140 \text{ km s}^{-1}$. We have made use of a time series of linear polarization

measurements of Sand 1 (A. F. J. Moffat et al. 2005, in preparation) to estimate the mass-loss rate of the W-R star. For this, we use the formalism developed by St-Louis et al. (1988). Their equation (6) gives

$$\dot{M}(M_{\odot} \text{ yr}^{-1}) = \frac{2.33 \times 10^{-7} A_p a (R_{\odot}) v_{\infty} (\text{km s}^{-1})}{(1 + \cos^2 i) f_c I},$$

where A_p is the half-amplitude of the major axis of the polarization ellipse in the Q - U plane, a is the semimajor axis of the orbit, v_{∞} is the terminal velocity of the wind of the W-R star, i is the orbital inclination, f_c is the fraction of the total light coming from the O star companion, and I is a constant given in the paper, which depends mainly on the wind velocity law. The polarization amplitude is $A_p = 0.071\%$. Using $a \sin i = 70 R_{\odot}$ from the adopted radial velocity amplitudes (see § 3.2.2), $v_{\infty} = 4200 \text{ km s}^{-1}$, $i = 40^{\circ}$, $f_c = 0.80$ from spectral types (see details in § 4.3), and $I = 7.75$ from St-Louis et al. (1988), we obtain $\dot{M}(\text{WO4}) \approx 0.8 \times 10^{-5} M_{\odot} \text{ yr}^{-1}$. We can therefore estimate the mass-loss rate of the O4 V star:

$$\dot{M}(\text{O4 V}) = \eta \frac{\dot{M}(\text{WO4}) v_{\infty}(\text{WO4})}{v_{\infty}(\text{O4 V})} \approx 2.4 \times 10^{-6} M_{\odot} \text{ yr}^{-1}.$$

This is very similar to the average value of the mass-loss rate of an O4 Galactic main-sequence star, $2.5 \times 10^{-6} M_{\odot} \text{ yr}^{-1}$, from Howarth & Prinja (1989).

Finally, again from equations (5) and (8), we obtain

$$v_{\text{str}} = \sqrt{\left(\frac{A}{\sin i}\right)^2 + \left[\frac{\text{FWHM}_{\text{max}} - \text{FWHM}_{\text{min}}}{2(1 - \cos i)}\right]^2} \approx 3820 \text{ km s}^{-1}. \quad (10)$$

The solid lines plotted in Figure 6 are the theoretical curves described by equations (2), (3), and (8) with the following parameters: $i = 50^{\circ}$, $\theta = 50^{\circ}$, and $v_{\text{str}} = 3000 \text{ km s}^{-1}$ (this corresponds to the best fit by eye: a curve with $i = 40^{\circ}$ and $v_{\text{str}} = 3820 \text{ km s}^{-1}$ does not represent the data as well; this is likely to be indicative of the errors involved using this technique). Although not a formal fit, it can be seen that they trace our measured values very well. The phase shift in this figure is $\delta\phi = 0.13$. The curves are very sensitive to i , θ , and v_{str} and cannot be reproduced with an inclination as low as 40° and the corresponding high values of θ and v_{str} . Once again, these results, although not implausible, must be taken with caution in view of the high level of noise in the optical spectra and the simplicity of the model.

4.3. A Combined Atmospheric Eclipse/Shock-Cone Emission Model

In an attempt to model the pronounced phase-locked line-profile variations, we have split all the available spectra into several groups, defined by a simple criterion: all the spectra in a given group should be closer in appearance to the group's mean spectrum than to any member of an adjacent group. This defines seven groups in total, with the number of spectra in each varying from 1 to 7. We average the spectra within each group, smooth the average spectrum by a 15 pixel wide running mean filter, and assign the corresponding average phase to each group.

As a framework for the model we use the SEI (Sobolev solution with exact integration) method developed by Lamers et al. (1987). In its initial form, the two-dimensional code cal-

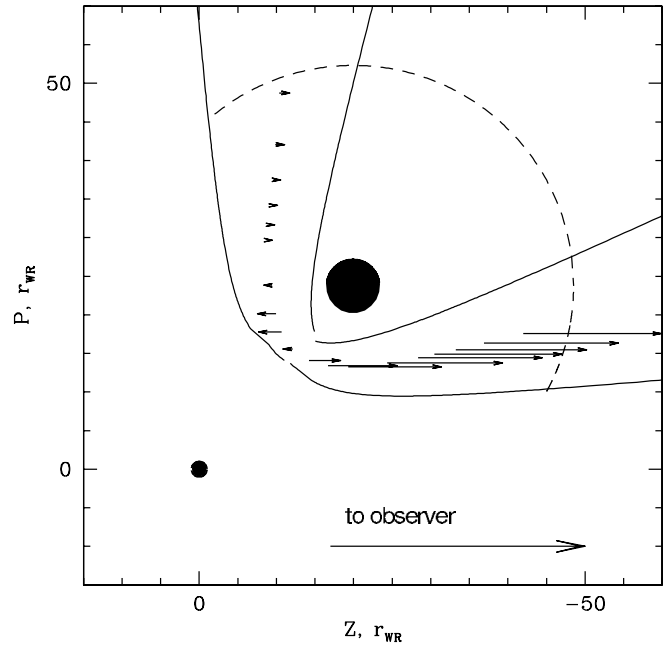


FIG. 11.—Schematic representation of the model used for line profile fitting, with the following geometric parameters: the orbital inclination $i = 40^{\circ}$, the orbital separation of the components $a = 103 R_{\odot}$, the asymptotic half-opening angle of the bow shock region $\theta = 35^{\circ}$, the starting distance of the bow shock emissivity at $\Delta r = 100 R_{\odot}$, and the characteristic density contrast in the WWC zone $\delta\rho = 4$ at $r < 1.5a$ and $\delta\rho = 30$ at $r \geq 1.5a$ (see text for more details).

culates line profiles in a moving atmosphere, specifying the total optical depth of the transition (either a single line or a doublet), two parameters characterizing the radial distribution of the optical depth, the ratio of collisional to radiative de-excitation, and the characteristic velocity of the assumed Gaussian turbulence, v_{turb} . The code adopts a velocity law in the traditional β form:

$$v(r) = v_0 + (v_{\infty} - v_0) \left(1 - \frac{R_{\star}}{r}\right)^{\beta},$$

with v_0 and β as free parameters. The resulting line profiles are normalized in velocity space such that $v_{\infty} \equiv 1$. The turbulent velocity is expressed in units of v_{∞} .

We generalize this approach to the case of a binary system where the wind-wind collision creates a zone with an additional emissivity component, treating the three-dimensional case in an approximate manner to facilitate the calculations: we project the corresponding surfaces of the bow shock onto the original two-dimensional surface in the radiation transfer calculations but keep a full three-dimensional treatment of the eclipsing phenomena, as well as the velocities of the gas streams in the WWC zone (for a geometric setup of the latter, see Lührs 1997). Hence, the model treats self-consistently the radiation transfer problem, accounting for three different regions: the unperturbed W-R wind, the wind-wind collision zone, and the wind of the O star confined by the WWC zone (Fig. 11). In addition, we account for O star light scattered by the W-R wind. Both stars are represented by disks of uniform brightness. The line profile component formed in the O star wind can be considered as a minor constituent: first, the O wind occupies a relatively small volume; second, the emissivity of the wind is low (relatively low density) compared to the W-R counterpart. Thus, we fix, rather

than derive, the parameters of the O star wind, assigning an optical depth distribution similar to that of the W-R wind (but naturally accounting for the difference in the radii of the components and allowing for the lower density of the O wind) and taking $v_\infty(\text{O star}) = (2140/4200)v_\infty = 0.51v_\infty(\text{W-R})$, $v_0(\text{O star}) = 0.01v_\infty(\text{O})$, and $\beta(\text{O star}) = 1.0$ (for the latter, see Massa et al. 2003). Along with estimated values of mass-loss rates, radii, and terminal velocities of both components, this leads to a ≈ 20 times lower normalized total optical depth of the O νI feature formed in the O star wind. Based on our estimates of mass-loss rates, radii, and terminal velocities of both components, we find that the expected density contrast in the W-R and O star winds is ≈ 25 .

Generalizing the initial spherically symmetric approach of SEI, we introduce a set of additional parameters for the components: their luminosity ratio, $L_O/L_{\text{W-R}}$; their radii, $R_{\text{W-R}}$ and R_O ; their orbital separation, a ; the orbital inclination i ; the asymptotic value of the opening half-angle of the bow shock region, θ ; and the value of the density contrast between the ambient W-R wind and the compressed gas in the bow shock zone, $\delta\rho_\infty$. In the present simulations this value was set constant throughout the zone. For the purpose of calculating the emissivity, we introduced a filling factor appropriate for the given density contrast. Although it may be easily introduced in the simulations, we do not distinguish between the O side and the W-R side of the bow shock zone. We find that the W-R side completely dominates the bow shock emissivity. Hence, separate treatment of the two parts would introduce one more free parameter that cannot be restricted. Moreover, the expected turbulence of the outflows would lead to substantial mixing of the W-R and O star sides at the distances considered in the simulations ($r \gtrsim a$, counting from the bow shock head). To account for the lack of line emissivity from the heated gas in the vicinity of the bow shock head, we introduce the starting distance Δr (measured from the bow shock head along the WWC zone) at which the shocked gas has cooled down sufficiently to start producing an emission line. For $r < \Delta r$, we set the density in the WWC zone to $\delta\rho = 4$. We use the fixed value for $a = 108 R_\odot$ from the adopted radial-velocity amplitudes and orbital inclination (see § 3.2.2). The shape of the WWC interface, as well as the velocity distribution of the shocked gas, is calculated using the analytic approach of Canto et al. (1996).

Searching for an optimal set of parameters, we use the O νI doublet as a principal testing ground, keeping the S νI $\lambda\lambda 933, 945$ profiles for a consistency check: the difficulty in defining a local continuum level, the very low flux level at $\lambda \lesssim 930 \text{ \AA}$, and blending prevent any meaningful quantitative comparison for the S νI profiles. The lack (Moffat et al. 1990) of detectable V-shaped minimum at $\phi \sim 0$ (W-R star in front; in fact, there is even an excess of continuum emission at $\phi \sim 0.0$) points to a rather low orbital inclination, $i < 60^\circ$. Hence, we start our search varying i from 60° downward, with a 5° decrement. Another restriction for the parameters comes from fitting the profiles at $\phi \sim 0.5$ (O star in front). Indeed, if the combination $(i + \theta)$ exceeds the critical value $\sim 90^\circ$, then due to the much lower v_∞ of the O wind, the high-velocity part of the absorption trough disappears because the W-R wind is being substituted by the O wind at $\phi \sim 0.5$. Apparently, this does not happen. We find that combinations of (i, θ) such as $(30^\circ, 45^\circ)$, $(35^\circ, 40^\circ)$, and $(40^\circ, 35^\circ)$ produce very similar best fits. This can be compared with our results of the simple geometrical model discussed in § 4.2, $\theta = 56^\circ$ when adopting $i = 40^\circ$. We use $i = 40^\circ$ and $\theta = 35^\circ$ as a basic reference model. Note that these smaller values of the orbital inclination and cone opening-angle

lead to mass-loss rates for the W-R and O stars of 8×10^{-6} and $0.7 \times 10^{-6} M_\odot \text{ yr}^{-1}$, respectively (see § 4.2). For the O star, this is much smaller than the Galactic mean value for stars of this spectral type. However, although not as extreme, this result is more compatible with the notion that the mass-loss rates of SMC O star dwarfs could be substantially lower than observed for Galactic counterparts (e.g., Martins et al. 2004). Fitting the emissivity component arising in the unperturbed W-R wind, we start from the phases where the influence of the WWC emissivity is minimal due to the projection of the WWC gas-stream velocities on the region occupied by the saturated P Cygni absorption trough, i.e., near $\phi \sim 0.5$. This allows us to find the first-iteration parameters describing the wind velocity law and the radial distribution of optical depth, as well as place restrictions on the luminosity ratio and the radii of the components. The fine-tuning is achieved by fitting the absorption trough at $\phi \sim 0.0$, i.e., at the phases when the WWC emission is distributed over the $v > 0$ part of the profile and the shape of the absorption part is most sensitive to the radial distribution of the optical depth. Then we introduce the additional emission component coming from the WWC zone and repeat the whole cycle again. We repeat this procedure for the range of phases used in creation of the average profile in each phase bin. This iterative fitting allows us to place the following limits on the principal parameters of the model:

1. The exponent of the W-R wind velocity law $\beta = 2.5 \pm 0.2$. This is compatible with recent estimates of β -values for W-R winds. For example, Ignace et al. (2003) have determined a value of $\beta = 2-3$ for the WN6 star HD 192163, using the *Infrared Space Observatory* continuum and He II emission-line fitting. Li et al. (2000) also require β -values larger than 1.5 to reproduce the observed mean polarization value as well as the ratio of polarimetric to photometric variability ($\sigma_{\text{pol}}/\sigma_{\text{phot}}$). In a study of inhomogeneities in W-R winds, Lépine & Moffat 1999 determined $20 < \beta R_{\text{star}} < 80$, which is incompatible with small values of β .
2. The starting W-R wind velocity $v_0/v_\infty = 0.16 \pm 0.02$ (which is close to the average value $v_0/v_\infty = 0.20-0.25$ for an early-type W-R star: Marchenko & Moffat 1999).
3. The characteristic turbulent velocity $v_{\text{turb}}/v_\infty = 0.09 \pm 0.02$ (again, a typical value; see Lépine & Moffat 1999).
4. The luminosity ratio $L_O/L_{\text{W-R}} = 3.5 \pm 0.5$. This can be compared with what is deduced from bolometric corrections and absolute visual magnitudes. Using a bolometric correction for O4 V stars in the LMC of $\text{BC}(\text{O4 V}) = -4.4$ (Massey & DeGioia-Eastwood 2000) and a V-band absolute magnitude of $M_V(\text{O4 V}) = -5.9$ (Schmidt-Kaler 1982), we obtain an O star luminosity of $L_{\text{O4}} = 1.0 \times 10^6 L_\odot$. For the WO4 star, we use a bolometric correction of $\text{BC}(\text{WO4}) = -6$ (Massey & DeGioia-Eastwood 2000) and a V-band absolute magnitude of $M_V(\text{WO4}) = -2.8$ (Schmidt-Kaler 1982), which yields a luminosity of $L_{\text{WO4}} = 0.25 \times 10^6 L_\odot$. The ratio is therefore $L_O/L_{\text{W-R}} \approx 4$, very similar to what we have deduced from our fits.
5. The radii of the components, $R_{\text{W-R}}/R_\odot = 3.5 \pm 0.3$ and $R_O/R_\odot = 12 \pm 5$ (apparently, the model is rather insensitive to the latter, keeping in mind the small impact of the emission component arising in the O star wind and the low orbital inclination of the system). We also note that, within the framework of the model, the “radius” defines a starting point of the calculations, i.e., the region of applicability of the prescribed wind velocity law. Apparently, the size of the hydrostatic W-R core could be substantially smaller.

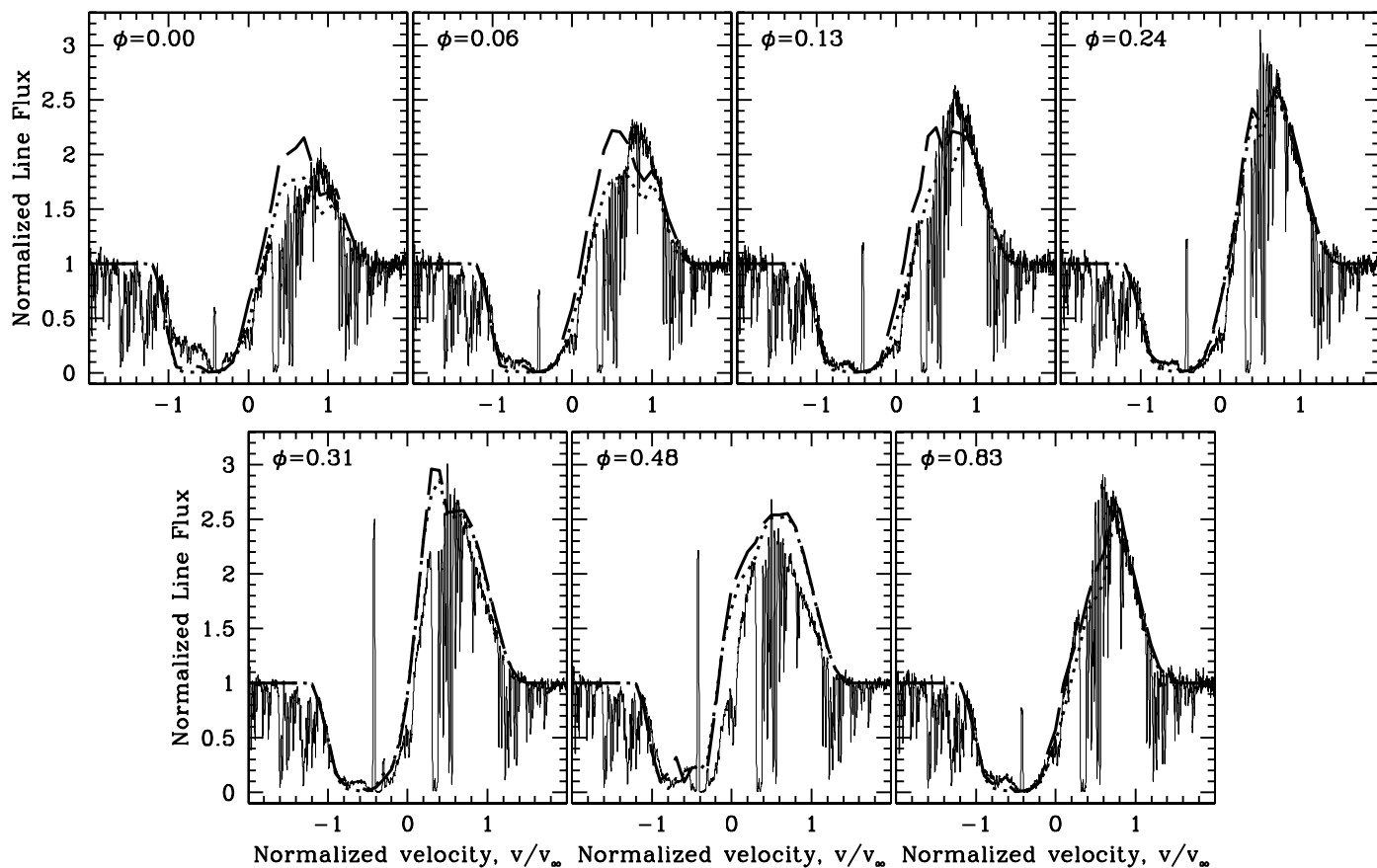


FIG. 12.—Phase-averaged, smoothed O VI profiles (solid lines) fitted with the modified SEI model: the long-dashed thick lines represent the model where all additional emission sources are accounted for, while the dotted lines show the model without the WWC emissivity and O star light back-scattered by the W-R wind.

6. The orbital inclination $i = 35^\circ \pm 5^\circ$ (not too far from the value derived earlier in § 4.2: $i = 47^\circ\text{--}58^\circ$) and the asymptotic value of the opening half-angle of the bow shock region $\theta = 40^\circ \pm 10^\circ$.

7. The value of the density contrast between the ambient W-R wind and the compressed gas in the bow shock zone, $\delta\rho_\infty = 30 \pm 5$, in favor of the latter. This value is kept fixed throughout the emissivity region, thus making no distinction between the trailing and leading regions of the bow shock. This roughly conforms to the density contrasts achieved in the hydrodynamic simulations (see next section). Note that this high density contrast favors more efficient cooling.

8. The starting distance of the bow shock emissivity $\Delta r/R_\odot = 100 \pm 40$.

9. The accepted $\theta = 35^\circ$ provides a range of velocities in the WWC zone that is smaller than the value of $v_{\text{str}} \sim 3820 \text{ km s}^{-1}$ derived in § 4.2 (eq. [10]): e.g., $v_{\text{str}} \sim 2350 \text{ km s}^{-1}$ at $r = a$ and $v_{\text{str}} \sim 2570 \text{ km s}^{-1}$ at $r = 2a$ (counting from the bow shock head). Note that a higher inclination value would lead to a smaller streaming velocity. For example, using a value of $i = 50^\circ$, would lead to more similar values ($\sim 2740 \text{ km s}^{-1}$).

The corresponding model is shown in Figure 12. Although the model follows the observed trends fairly well, there are some noticeable deviations: at $\phi = 0.48$ the observed profile shows a lack of emission at $v > 0.5v_\infty(\text{W-R})$. This lacking component is replaced by a substantially enhanced (relative to the model fit) emissivity at $\phi = 0.06$. Taken together, these events may point to a general, large-scale asymmetry of the

W-R wind that is not accounted for by the model. Gravitational tides from the massive and relatively close O star could provoke the asymmetry. We also note that at $\phi = 0.24$ the redshifted, high-velocity part of the extra emission component arising in the WWC zone is not matched by the model. In view of the configuration of the system at $\phi = 0.24$, we suggest that this could be a result of higher turbulent velocities in the WWC zone, which are not matched by the model, as the model assigns a similar characteristic turbulent velocity to the W-R wind as to the gas in the WWC zone.

The modified SEI code also has a built-in possibility to calculate light curves, taking into account two sources of opacity: electron scattering, and free-free absorption. We use the code to calculate the phase-dependent flux at $\lambda = 1000 \text{ \AA}$ for a binary with $\dot{M}(\text{WO4}) = 0.8 \times 10^{-5} M_\odot \text{ yr}^{-1}$ and the rest of the parameters provided by the profile simulations. The calculated curve (see Fig. 2, bottom panel) shows a maximum at $\phi = 0.6$ (this correspond to $\phi = 0.5$ in the model: recall that there is a phase shift of $\delta = -0.1$ between the Bartzakos et al. [2001] phases and ours). However, the calculated light curve is much wider and the amplitude is much smaller. Furthermore, the model curve is symmetric around $\phi = 0.6$, while the observations seem to show a slower rise and a sharp decline. The unaccounted additional sources of opacity (e.g., ions of Fe VI or VII) could explain the higher amplitude; the observed asymmetry could be produced by the Coriolis-shifted bow shock cavity. More surprising is the seeming lack of atmospheric eclipses in the observations while the model shows modest fading of the system around $\phi = 0.1$. We are not able to explain

this phenomenon. However, we note that it comes along with other anomalies observed during atmospheric eclipses: the strange behavior of the C III line (Fig. 9), the possible brightening of the system registered in the optical data, and the partial filling of the P Cygni absorption trough of O VI at $\phi = 0.0$ (Fig. 12).

The selective wind eclipse provides a strong constraint on the position of the O star at a given phase. Indeed, if the W-R wind is not dramatically asymmetric, the eclipse should be symmetric around the phase at which the O star is farthest behind the W-R star. We found that this symmetry point is at $\phi = 0.0$, as expected. Consequently, there cannot be a delay between the UV excess emission and the orbital position of the O star. This means that the O VI lines (for example) should be formed not too far downstream along the shock cone.

4.4. Radiative Braking

The analysis carried out in the previous sections assumes that the two stellar winds collide at terminal velocity. This may not necessarily be the case here. In fact, Gayley et al. (1996, 1997) have shown that a rather sudden *radiative braking* of the W-R wind is likely to be a widespread phenomenon among W-R+O binaries. This occurs when the W-R wind is decelerated by the opposing radiative momentum flux it encounters as it approaches the bright O star companion. This process is aided by the fact that the W-R wind has a higher opacity than that of the O star wind. In order to estimate if radiative braking occurs in Sand 1, we need to place it on Figure 5 of Gayley et al. (1997). This figure plots the scaled momentum ratio ($P_{W-R/O}/P_{rb}$) as a function of the scaled binary separation (D/D_{rb}). However, an important assumption in this figure is that $\alpha = 0.5$ (where α is the exponent in the force-multiplier term in the theory of Castor et al. 1975, hereafter CAK). If the value of α required to obtain the observed mass loss and wind speeds of the stars is different from this value, the strength of the radiative braking can be substantially altered.

We therefore have adjusted the α and k parameters to obtain the desired mass loss and wind speeds of each star, given specified stellar parameters.² SMC metal abundances (solar/10) were assumed for the O4 star, whereas for the WO4 star we assumed the following mass fractions: $X_{He} = 0.22$, $X_C = 0.52$, $X_O = 0.25$ (Kingsburgh et al. 1995). While there is some uncertainty concerning elemental abundances in WO stars, adopting the abundances determined for Sand 2, Sand 4, or Sand 5 (Kingsburgh et al. 1995) makes little difference to our results.

The stellar parameters are shown in Table 3. The mass-loss rates, stellar radii, and luminosities are from §§ 4.2 and 4.3, while the terminal velocities are from Kingsburgh et al. (1995) and the masses from our new orbit presented in § 3.2.2. Here we have again adopted $i = 40^\circ$. We point out that the adopted luminosity and radius lead to an effective temperature for the O4 V star of $T_{eff} = 52$ kK that is higher than expected for this spectral type (Martins et al. 2004). Note that k is normalized in terms of the specific electron opacity to Thomson scattering, $\sigma_e = \sigma_T/m_H$, and a fiducial ion thermal speed, v_{th} (see Abbott 1982, and eq. [14]). By convention, these quantities reflect solar abundances, but in this work we have used the actual wind abundances to define σ_e . For the WO4 wind we find $\sigma_e = 0.20$,

² We therefore make the implicit assumption that CAK theory can describe the winds of W-R stars. While this may be somewhat inappropriate at this time, it does allow a model of the wind to be constructed. Since this work started, we have learned that a model for the *full* dynamical structure of W-R winds has been obtained for the first time (Gräfener & Hamann 2005).

TABLE 3
STELLAR PARAMETERS

Quantity	WO4	O4	O4 ver. 2
Mass-loss rate \dot{M} ($M_\odot \text{ yr}^{-1}$).....	8.0×10^{-6}	2.4×10^{-6}	5.0×10^{-7}
Terminal speed v_∞ (km s^{-1}).....	4200	2140	2170
Radius R (R_\odot).....	3.5	12.0	...
Mass M (M_\odot).....	15.9	45.5	...
Luminosity L (L_\odot).....	2.5×10^5	1.0×10^6	...
Hydrogen mass fraction X	0.0	0.720	...
Helium mass fraction Y	0.22	0.278	...
Metal mass fraction Z	0.78	0.002	...
CAK exponent α	0.62	0.58	...
CAK constant k	0.76	0.09	0.037

while for the O4 wind $\sigma_e = 0.34$. The average mass per particle is $1.80m_H$ in the WO4 wind and $0.60m_H$ in the O4 wind. We have also considered a lower mass-loss rate for the O4 star, since there is some evidence that the mass-loss rates of O stars in the SMC are lower than their Galactic counterparts (Martins et al. 2004). This leads to a change in value for k , as shown in Table 3.

An important unknown in determining the degree of radiative braking is the strength at which the O star radiation field couples to the oncoming W-R wind (because of this uncertainty, Owocki & Gayley [1995] showed numerical results for the braking in V444 Cygni for three different values of the line opacity parameter—we shall henceforth refer to this parameter as k_c). This uncertainty is based on the fact that the driving of massive star winds depends on several factors, namely, the elemental abundance of the wind, its ionization (and stratification), and the photon spectrum of the star. We can speculate further on the value of k_c . If the wind driving of massive stars is, for a given spectrum of the radiation field, due mainly to the abundance of Fe, then we can expect that $k_c = k_{O4}$ (since the Fe abundance in both the O4 and WO4 stars will be identical); but if it depends on the elemental abundance of the W-R wind, then $k_c = k_{WO4}$. On the other hand, Abbott (1982) suggests that the radiative force due to line driving depends on the overall metallicity of the wind and scales as $Z^{1-\alpha}$. The ratio of Z between the WO4 and O4 winds means that in this scenario

$$k_c = \left(\frac{Z_{WO4}}{Z_{O4}} \right)^{1-\alpha} k_{O4}. \quad (11)$$

Putting in the appropriate values, we find that $k_c \approx 10.87k_{O4} = 0.98$, which is larger than the value we estimated for $k_{WO4} (= 0.76)$. This seems to indicate that the coupling between the radiation field of the O star and the W-R wind is stronger than the radiation field of the W-R star with its own wind. While this may be possible, strong braking is already obtained with $k_c = k_{WO4}$, so we restrict our models to $k_c \leq k_{WO4}$.

The final quantity that we must specify before we can investigate the strength of radiative braking in this system is the distance between the stars. We therefore have assumed that the inclination of the system is 40° (see § 4.2), which means that the stellar separation, $a = 108 R_\odot$.

Using the above parameters and those in Table 3, we find that the braking radius (defined in eq. [18] of Gayley et al. 1997) is $x_b = 0.11$ and 0.32 for $k_c = 0.09$ and 0.76 , respectively (the scaled radius $x_b = r/D$). The deceleration of the WO4 wind is

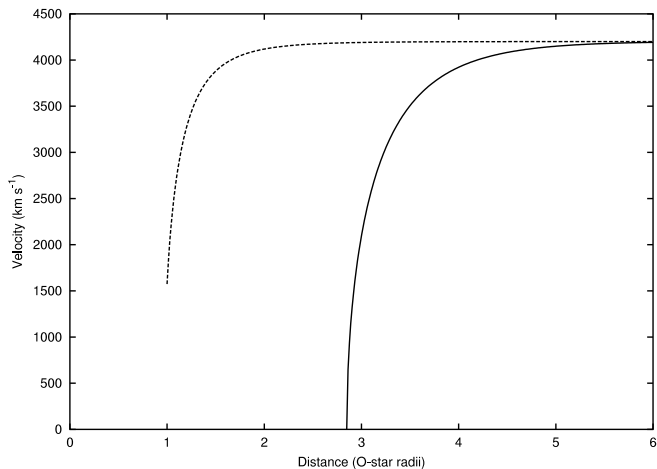


FIG. 13.—Effect of radiative braking on the velocity of the WO4 wind as it approaches the O4 star. The WO4 wind is assumed to have been accelerated to its terminal speed of 4200 km s^{-1} , and it impinges on the O star from right to left. We adopt $k_{\text{WO4}} = 0.76$ and $k_{\text{O4}} = 0.09$ as the line strength parameter for the WO4 and O4 stars, respectively. Results for two different strengths of coupling are shown: $k_c = 0.09$ and 0.76 . As k_c increases, the braking of the WO4 wind becomes stronger and occurs further from the O star photosphere.

shown in Figure 13, where we have used equation (16) in Gayley et al. (1997) with $\alpha = 0.58$ and $\sigma_e = 0.20$. Clearly, there is strong braking if the coupling is dependent on the overall metallicity in the WO4 wind ($k_c = 0.76$) and more moderate braking if the coupling is mainly dependent on the Fe abundance ($k_c = 0.09$).

This analysis has provided an indication of the wind dynamics in Sand 1. However, to test the constraints determined in the previous section (i.e., the twin conditions of $i + \theta < 90^\circ$ and a cooling length along the shock cone of $\approx 100 \pm 40 R_\odot$), we will need to turn to a hydrodynamic model of the wind collision. This is discussed in the next section.

4.5. Cooling Times: A Hydrodynamic Model

The colliding wind models were calculated using PICA, a second-order-accurate Godunov scheme utilizing adaptive mesh refinement (AMR). PICA is closely related to COBRA (Falle & Giddings 1993), the latter having been applied to such diverse problems as the formation of tails in clump-wind interactions (Falle et al. 2002) and to the interaction of a supernova remnant with the wind from an active galactic nucleus (Pittard et al. 2003). The AMR capability of PICA is particularly well suited to calculations of the acceleration of stellar winds through radiative driving since the evaluation of velocity gradients is computationally demanding. PICA uses a hierarchy of grids $G^0 \dots G^N$ such that the mesh spacing on grid G^n is $\Delta x_0/2^n$. Grids G^0 and G^1 cover the whole domain, but the finer grids only exist where they are needed. The solution at each position is calculated on all grids that exist there, and the difference between these solutions is used to control refinement. In order to ensure Courant number matching at the boundaries between coarse and fine grids, the time step on grid G^n is $\Delta t_0/2^n$, where Δt_0 is the time step on G^0 . Such a hierarchical grid structure improves the efficiency by confining the fine grids to where they are needed. Radiative cooling is included via the method of operator splitting and is calculated as an optically thin plasma in ionization equilibrium. The stellar winds are modeled as ideal gases with adiabatic index $\gamma = 5/3$.

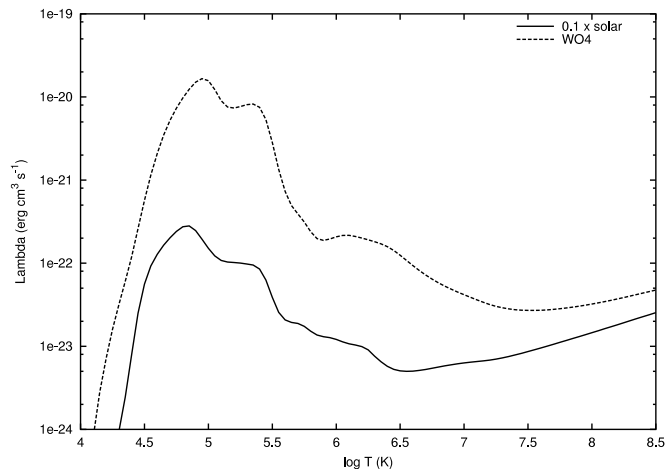


FIG. 14.—Cooling curves for the wind material of the O4 star (solid curve) and the WO4 star (dashed curve). The ordinate is a measure of the cooling rate ($\text{ergs cm}^3 \text{ s}^{-1}$) as a function of gas temperature. For a given density, the WO4 material cools more quickly throughout the temperature range 10^4 – 10^9 K.

In our simulations we assumed axisymmetry and computed the flow on a three-dimensional grid—the neglect of orbital motion should have little effect on the cooling times and lengths. We adopted the wind and system parameters deduced in the previous sections. Cooling rates for the material in each wind were calculated from the MEKAL thermal plasma code (Mewe et al. 1985; Kaastra 1992) distributed in XSPEC (ver. 11.2.0). Since there is no hydrogen in the wind of the WO4 star, we have parameterized the cooling as

$$\left[\frac{dE}{dt} \right]_{\text{rad}} = \left(\frac{\rho}{m_{\text{H}}} \right)^2 \Lambda. \quad (12)$$

The value of Λ as a function of temperature for the two winds is shown in Figure 14.

Since this is a short-period system with high wind speeds, inverse Compton cooling of the shocked gas by UV photons from the stellar radiation fields is likely to be important. We have therefore included such cooling as (see White & Chen 1995)

$$\left[\frac{dE}{dt} \right]_{\text{ic}} = \frac{4\sigma_{\text{T}}k}{m_e c} n_e U_{\text{ph}} T, \quad (13)$$

where n_e is the electron number density and U_{ph} is the photon energy density. Inverse Compton cooling dominates radiative cooling at high temperatures, and vice versa.

The acceleration of *both* winds is calculated in our simulations. Since this demands Cartesian (r, z) coordinates, we are not able to obtain the high resolution near the stars that can be achieved with a spherical polar (r, θ) coordinate system. As a consequence, we do not resolve the sonic point in our simulations and must start the flow from the stars supersonically. This, of course, means that the mass-loss rate of the stars (and the wind terminal speed) is not fully self-consistent with the presence of a neighboring star. We aim to improve this feature in our model in the near future.

To initiate the winds we fix the density and velocity within an annulus of two cell widths around each star. The computation of the line acceleration is based on a local Sobolev (1960) treatment of the line transport, following the standard CAK

formalism developed for single OB winds. The vector radiative force per unit mass, g^{rad} , is computed from an integral of the intensity $I(\mathbf{n})$ times the projected velocity gradient along directional vectors \mathbf{n} within the solid angle covering the stellar disk,

$$\mathbf{g}^{\text{rad}} = \frac{\sigma_e^{1-\alpha} k}{c} \oint I(\hat{\mathbf{n}}) \left[\frac{\hat{\mathbf{n}} \cdot \nabla(\hat{\mathbf{n}} \cdot \mathbf{v})}{\rho v_{\text{th}}} \right]^\alpha \hat{\mathbf{n}} d\Omega. \quad (14)$$

The integration over solid angle is performed with eight directional vectors. The line and continuum radiative forces and the gravitational force are calculated for both stars. Further details concerning the line force calculations can be found in Gayley et al. (1997), and previous work with this setup is shown in Pittard (1998) and Pittard & Stevens (1999).

In Figure 15 we show G^3 , density, velocity, and temperature plots from a hydrodynamic simulation with $\dot{M}_{\text{O4}} = 2.4 \times 10^{-6} M_\odot \text{ yr}^{-1}$ and $k_c = 0.09$. The WO4 star is located in the bottom left corner of each plot. The radius of the O4 star is equivalent to the width of 48 cells, so that the edge of the annulus fixing the O4 wind has a radius of $\approx 1.04 R_{\text{O4}}$. As can be seen, the shock does not impact the surface of the O4 star. This is due to the fact that the winds are able to obtain momentum balance, in this case when radiative braking is negligible (see Fig. 13). The collision speed on the symmetry axis is 3800 km s^{-1} , which indicates that the WO4 wind has not quite accelerated to terminal speed over the distance between the stars.

The other notable feature of this model is the high-density stream of cool (10^4 K) gas within the wind collision region. This stream is slow moving ($v \sim 100\text{s of km s}^{-1}$ near the shock apex) and is thus subject to a high shear velocity with the fast-moving shocked WO4 material. The strong growth of Kelvin-Helmholtz (and other) instabilities breaks up the stream into dense clumps, which are advected with the shocked flow. Some of these clumps subsequently find themselves in the shocked WO4 flow, where they are subject to rapid ablation. The mixing of the cold gas from the clumps with the hotter gas surrounding them causes the latter to cool,³ and the amount of cool WO4 material increases as one moves downstream. The mass of the resulting cold WO4 material may then approach (or even exceed) the mass of cold O4 material. In any case, since the oxygen abundance per unit mass is much higher in the WO4 material than in the O4 material, it is the WO4 wind that provides the clear majority of O VI ions (even though most of its shocked wind does not cool very rapidly).

While the colder gas is generated close to the stars, O VI emission requires gas at intermediate temperatures. Since the mass of cold material (which can mix with the hotter gas to create material at intermediate temperatures) increases with downstream distance, while the density of the intermediate-temperature gas decreases with downstream distance due to the geometric expansion of the flow, it is possible that the O VI emissivity peaks at some finite distance downstream. This may explain the finding in the previous section that the O VI emission appears to start at a downstream distance of approximately $100 R_\odot$. In contrast, shocked WO4 material that is not in contact with cool clumps will have a very long cooling length, which

we estimate as $\approx 2000 R_\odot$. Another fact that may contribute to reducing our predicted cooling lengths is the clumpiness of the W-R and (perhaps to a lesser extent) O star winds. The fate of such clumps is discussed in J.-M. Pittard et al. (2005, in preparation), and a first numerical model of the collision of clumped stellar winds is presented by Walder & Folini (2002). They found that although it is likely that many clumps would be destroyed by their passage through the colliding-wind shock cone, their presence may lead to increased turbulence in the interaction region, which in turn will tend to make the gas more inhomogeneous. A higher contrast between hot and cold regions is expected; i.e., cool clumps should be denser and the hotter gas of lower density. This could help increase the efficiency of the cooling and therefore reduce the cooling lengths.

There is in fact one detail that may help to explain why we detect a phase shift in the optical C IV (predominantly recombination) line compared to the UV O VI (scattering) transitions. When modeling the O VI profiles with the modified SEI code, we find that a significant part of the additional emission (above 50%) comes from the O star continuum flux back-scattered by the W-R wind. This proportion may be much lower in a line formed via recombination, due to a higher sensitivity of the line to the large density contrast in the bow shock zone. Hence, considering that the extra emission is formed from two components (the back-scattered O light with no phase shift and the phase-shifted emission coming from the distant zone in the bow shock), we find that the C IV $\lambda 5808$ line may very well exhibit a relatively high phase shift.

The half opening-angle of the wind-collision region (measured as an average over the cool clumps within the shocked flow) in our model is $\approx 55^\circ$. This angle, combined with the adopted inclination of the system, is in rough agreement with the constraint determined in the previous section (i.e., that $i + \theta + d\theta \lesssim 90^\circ$). In contrast, we find that a model with a higher value of k_c yields a much higher value of θ . For this reason, we exclude the models where the coupling between the O star radiation field and the W-R wind either depends on the elemental abundance of the W-R wind or scales as $Z^{1-\alpha}$, as suggested by Abbott (1982).

We have also calculated models with a reduced mass-loss rate for the O star (see Table 3). In this case, $k_c = k_{\text{O4}} = 0.037$ if the acceleration is mainly dependent on the Fe abundance. We find one behavior that is different from our earlier results computed with $\dot{M} = 2.4 \times 10^{-6} M_\odot \text{ yr}^{-1}$ and $k_c = 0.09$ —the WO4 wind now impacts the surface of the O4 star as radiative braking is not strong and the momentum balance is not attained. On the other hand, we still find a dense cold stream of O4 material that is stripped from it, and this subsequently breaks up into clumps that mix with the shocked WO4 gas and intermediate temperatures are obtained.

Ideally, we would like to investigate the emissivity of the intermediate-temperature gas created by the mixing of the hot and cold gas in the wind collision region. In particular, we would like to determine the downstream distance at which the O VI emission peaks to compare against the results obtained from our other modeling. However, there are a number of good reasons why we are not yet in a position to carry out an investigation of this sort at the present time. First, as we have already noted, there are numerical issues associated with the cooling of hot gas next to cold clumps. Second, our simulation does not resolve the small spatial scales associated with these clumps, e.g., Klein et al. (1994) determined that of order 100 cells per clump radius were needed to properly model the destruction of clumps overrun by an astrophysical shock. And third, the

³ There are, in fact, some numerical issues associated with this effect—a hot pulse in a cool medium is “eaten away” from the sides during advection across a hydrodynamic grid since the numerical scheme will construe cells to be at an intermediate temperature (where radiative cooling may be maximized) between the hot and cold phases.

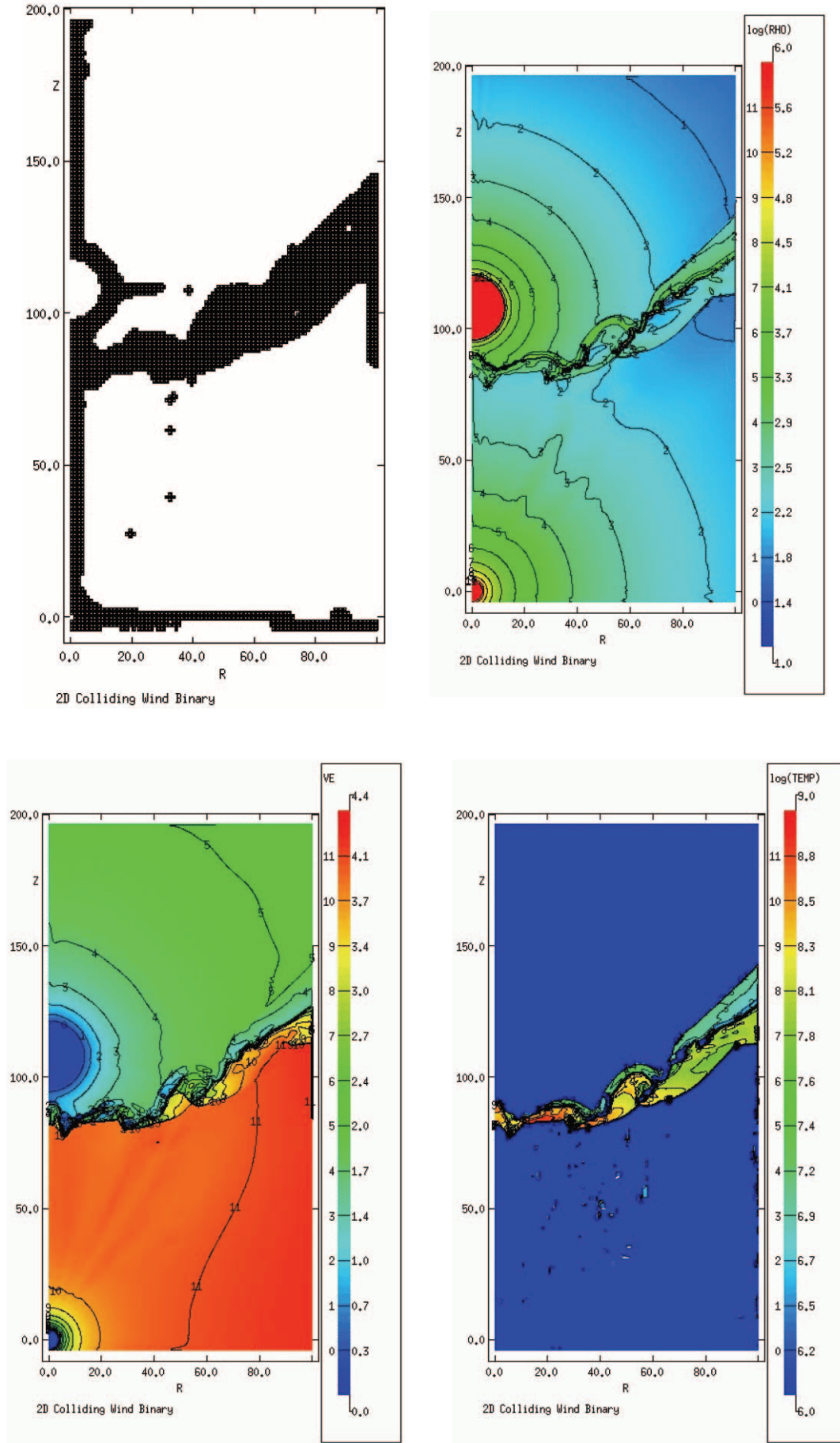


FIG. 15.— G^3 (top left), density (top right), velocity (bottom left), and temperature (bottom right) plots of the wind-wind collision in Sand 1, where $\dot{M}_{04} = 2.4 \times 10^{-6} M_{\odot} \text{ yr}^{-1}$ and $k_c = 0.09$. The units on the axes are R_{\odot} , while the unit of density is $1.74 \times 10^{-17} \text{ g cm}^{-3}$, the unit of velocity is 1000 km s^{-1} , and the unit of temperature is kelvins.

TABLE 4
ORBITAL AND STELLAR PARAMETERS

Parameter	Modified SEI Model	Other Models
Orbital inclination, i (deg).....	35 ± 5	40 ± 10^a
Half opening angle θ (deg).....	40 ± 10	56^a
Streaming velocity along the cone v_{strm} (km s^{-1}).....	2570 (at $r = 2a$)	3820^a
Starting bow shock emissivity distance Δr (R_{\odot}).....	100 ± 40	1435 (WO4), 0 (O4) ^b
Shock/ambient wind density contrast δ_{∞}	30 ± 5	...
O star radius R_{O} (R_{\odot}).....	12 ± 5	...
W-R star radius $R_{\text{W-R}}$ (R_{\odot}).....	3.5 ± 0.3	...
Luminosity ratio $L_{\text{O}}/L_{\text{W-R}}$	3.5 ± 0.5	4.0^c
Characteristic turbulent velocity of W-R wind v_{turb}	$0.09v_{\infty} \pm 0.02v_{\infty}$...
Starting W-R wind velocity $v_{\text{O}}/v_{\text{W-R}}$	$0.16v_{\infty} \pm 0.02v_{\infty}$...
β -law exponent of the W-R star β	2.5 ± 0.2	...

^a From the Lührs (1997) model.

^b From the hydrodynamic model. This value assumed no mixing between the WO4 gas and the cold O4 gas, which invariably will reduce Δr .

^c From spectral types.

nature of the mixing is both quantitatively and qualitatively different in three dimensions.

5. CONCLUSIONS

In this paper we have discussed the variable far-ultraviolet spectra of the unique W-R+O binary Sand 1. This SMC (therefore low-metallicity) binary includes one of the rare W-R stars of WO subtype, which represent what is thought to be the most evolved evolutionary stage of massive stars before a gravitational-collapse supernova. This star also has one of the fastest, stable, sustained winds ($v_{\infty} = 4200 \text{ km s}^{-1}$) among W-R stars. The companion, an O4 star, is also massive and hot.

We have shown that all major P Cygni profiles in the spectrum (O VI $\lambda\lambda 1032, 1038$; S VI $\lambda\lambda 933, 945$; C III $\lambda 977$; and C IV + C III $\lambda\lambda 1068, 1075$) are variable and concluded that the changes are caused by two physical processes.

First, there is excess emission from a shock cone formed as a result of the collision between the two stellar winds. At the head of the shock-cone, X-rays must be produced, and therefore we originally expected the O VI doublet to be formed close by and therefore to trace a cone opening angle that would be larger than that of other lines expected to be formed in the linear part of the cone further downstream. Inspection of the variability patterns reveals that this is not the case, as the spectra show that all lines vary in concert. As the shock cone is tied to the O star, it is carried around in the orbit and we can thus view it from different directions and therefore at varying velocities, simply via the Doppler effect. This is what causes the periodic spectral variability as a function of phase. To model the excess emission, we have first applied the simple geometrical model developed by Lührs (1997). From this analysis and adopting an orbital inclination of $i = 40^\circ$, we deduce the following parameters: the half-opening angle $\theta = 56^\circ$ and the flow velocity along the shock cone, $v_{\text{str}} = 3820 \text{ km s}^{-1}$.

We have also constructed models in which the radiative driving of the winds is calculated—in a binary system this can lead to the occurrence of effects such as radiative inhibition and braking. In Sand 1, the coupling of the O4 radiation field to the WO4 wind is dependent on the value of the line-opacity parameter, k_c . Our models eliminate the possibility that $k_c = k_{\text{WO4}}$, since the opening angle of the collision region would be far too large. In this particular case, a line-opacity parameter that scales as $Z^{1-\alpha}$ is larger than k_{WO4} and therefore that value is also excluded for the same reasons.

The shocked O4 wind rapidly cools and mixes with the hotter WO4 gas, causing the WO4 gas to cool more efficiently. The intermediate temperatures that are then obtained may be responsible for the observed O VI emission and the fact that we find that the emissivity peaks at a distance of approximately $100 R_{\odot}$ downstream.

The second physical process responsible for the observed variability is selective wind eclipses. This occurs when the O star's continuum emission is absorbed by ions in the W-R wind.

The two phenomena occur concurrently, and the resulting variations are intertwined in the spectra. Therefore, in order to determine parameters as accurately as possible, the two effects must be modeled together. To do this, we have produced a line-emission model based on the method developed by Lamers et al. (1987). Our model includes emission from the two winds and from the shock cone, selective wind eclipses, as well as back-scattering of the O star light by the W-R wind. Comparison of the calculated global profiles with observations has allowed us to deduce several parameters intrinsic to the stars and their winds, as well as to the binary system. We summarize them in Table 4.

In conclusion, the FUSE data have not only helped us determine important stellar, wind, and binary parameters but also to begin carrying out more detailed models of wind-wind collisions in W-R+O binaries. In doing so we have found that this involves many complex phenomena that we are just beginning to understand.

N. S. L. and A. F. J. M. are grateful for financial assistance from the Natural Sciences and Engineering Council (NSERC) of Canada, and Le fonds québécois de la recherche sur la nature et les technologies (FQRNT) of Quebec. J. M. P. is grateful for funding from the Particle Physics and Astronomy Research Council (PPARC) of the UK. This work was partially supported by the NASA research grant NAG5-13716.

It is also with great pleasure that we thank Alex Fullerton, one of our two official Canadian astronomer contacts with the FUSE project, who has patiently run our data set through several versions of the CALFUSE pipeline. We thank the anonymous referee for a careful reading of the manuscript and for constructive comments.

REFERENCES

- Abbott, D. C. 1982, *ApJ*, 259, 282
- Auer, L. H., & Koenigsberger, G. 1994, *ApJ*, 436, 859
- Barlow, M. J., & Hummer, D. G. 1982, in *IAU Symp. 99, Wolf-Rayet Stars: Observations, Physics, Evolution*, ed. C. W. H. de Loore & A. J. Willis (Dordrecht: Reidel), 387
- Bartzakos, P., Moffat, A. F. J., & Niemela, V. S. 2001, *MNRAS*, 324, 33
- Breysacher, J., & Westerlund, B. E. 1978, *A&A*, 67, 261
- Canto, J., Raga, A. C., & Wilkin, F. P. 1996, *ApJ*, 469, 729
- Castor, J. I., Abbott, D. C., & Klein, R. I. 1975, *ApJ*, 195, 157 (CAK)
- Crowther, P. A., De Marco, O., & Barlow, M. J. 1998, *MNRAS*, 296, 367
- Crowther, P. A., et al. 2000, *ApJ*, 538, L51
- Falle, S. A. E. G., Coker, R. F., Pittard, J. M., Dyson, J. E., & Hartquist, T. W. 2002, *MNRAS*, 329, 670
- Falle, S. A. E. G., & Giddings, J. R. 1993, in *Numerical Methods for Fluid Dynamics 4*, ed. K. W. Morton & M. J. Baines M. J. (Oxford: Clarendon), 335
- Fullerton, A. W., Gies, D. R., & Bolton, C. T. 1996, *ApJS*, 103, 475
- Gayley, K. G., Owocki, S. P., & Cranmer, S. R. 1996, *Rev. Mex. A.A. Ser. Conf.*, 5, 68
- . 1997, *ApJ*, 475, 786
- Gräfener, G., & Hamann, W.-R. 2005, *A&A*, 432, 633
- Herald, J. E., Schulte-Ladbeck, R. E., Eenens, P. R. J., & Morris, P. 2000, *ApJS*, 126, 469
- Hoopes, C. G., Sembach, K. R., Howk, J. C., Savage, B. D., & Fullerton, A. W. 2002, *ApJ*, 569, 233
- Howarth, I. D., & Prinja, R. K. 1989, *ApJS*, 69, 527
- Ignace, R., Quigley, M. F., & Cassinelli, J. P. 2003, *ApJ*, 596, 538
- Kaastra, J. S. 1992, *An X-Ray Spectral Code for Optically Thin Plasmas* (Internal SRON-Leiden Rep., updated ver. 2; Leiden: SRON)
- Kingsburgh, R. L., Barlow, M. J., & Storey, P. J. 1995, *A&A*, 295, 75
- Klein, R. I., McKee, C. F., & Colella, P. 1994, *ApJ*, 420, 213
- Lamers, H. J. G. L. M., Cerruti-Sola, M., & Perinotto, M. 1987, *ApJ*, 314, 726
- Lamontagne, R., Moffat, A. F. J., Drissen, L., Robert, C., & Matthews, J. M. 1996, *AJ*, 112, 2227
- Lépine, S., & Moffat, A. F. J. 1999, *ApJ*, 514, 909
- Li, Q., Brown, J. C., Ignace, R., Cassinelli, J. P., & Oskinova, L. M. 2000, *A&A*, 357, 233
- Lührs, S. 1997, *PASP*, 109, 504
- Maeder, A., & Meynet, G. 1994, *A&A*, 287, 803
- Marchenko, S. V., & Moffat, A. F. J. 1999, *A&A*, 341, 211
- Martins, F., Schaerer, D., Hillier, D. J., & Heydari-Malayeri, M. 2004, *A&A*, 420, 1087
- Massa, D., Fullerton, A. W., Sonneborn, G., & Hutchings, J. B. 2003, *ApJ*, 586, 996
- Massey, P., Waterhouse, E., & DeGioia-Eastwood, K. 2000, *AJ*, 119, 2214
- Mewe, R., Gronenschild, E. H. B. M., & van den Oord, G. H. J. 1985, *A&AS*, 62, 197
- Moffat, A. F. J., Breysacher, J., & Seggewiss, W. 1985, *ApJ*, 292, 511
- Moffat, A. F. J., Niemela, V. S., & Marraco, H. G. 1990, *ApJ*, 348, 232
- Monnier, J. D., Tuthill, P. G., & Danchi, W. C. 1999, *ApJ*, 525, L97
- Moos, H. W., et al. 2000, *ApJ*, 538, L1
- Nugis, T., Crowther, P. A., & Willis, A. J. 1998, *A&A*, 333, 956
- Owocki, S. P., & Gayley, K. G. 1995, *ApJ*, 454, L145
- Pittard, J. M. 1998, *MNRAS*, 300, 479
- Pittard, J. M., Dyson, J. E., Falle, S. A. E. G., & Hartquist, T. W. 2003, *A&A*, 408, 79
- Pittard, J. M., & Stevens, I. R. 1999, in *IAU Symp. 193, Wolf-Rayet Phenomena in Massive Stars and Starburst Galaxies*, ed. K. A. van der Hucht, G. Koenigsberger, & P. R. J. Eenens (ASP: San Francisco), 386
- Prinja, R. K., Barlow, M. J., & Howarth, I. D. 1990, *ApJ*, 361, 607
- Puls, J., et al. 1996, *A&A*, 305, 171
- Richter, P., Savage, B. D., Wakker, B. P., Sembach, K. R., & Kalberla, P. M. W. 2001, *ApJ*, 549, 281
- Sahnow, D. J., et al. 2000, *ApJ*, 538, L7
- Schmidt-Kaler, Th. 1982, in *Stars and Star Clusters*, ed. K. Schaiffers & H. H. Voigt (Berlin: Springer), 41
- Seggewiss, W., Moffat, A. F. J., & Lamontagne, R. 1991, *A&AS*, 89, 105
- Sobolev, V. V. 1960, *Moving Envelopes of Stars* (Cambridge: Harvard Univ. Press)
- St-Louis, N., Moffat, A. F. J., Drissen, L., Bastien, P., & Robert, C. 1988, *ApJ*, 330, 286
- St-Louis, N., Willis, A. J., & Stevens, I. R. 1993, *ApJ*, 298
- Tumlinson, J., et al. 2002, *ApJ*, 566, 857
- Tuthill, P. G., Monnier, J. D., & Danchi, W. C. 1999, *Nature*, 398, 487
- Usov, V. V. 1992, *ApJ*, 389, 635
- Walborn, N. R., Fullerton, A. W., Crowther, P. A., Bianchi, L., Hutchings, J. B., Pellerin, A., Sonneborn, G., & Willis, A. J. 2002, *ApJS*, 141, 443
- Walder, R., & Folini, D. 2002, in *ASP Conf. Ser. 260, Interacting Winds from Massives Stars*, ed. A. F. J. Moffat & N. St-Louis (San Francisco: ASP), 595
- White, R. L., & Chen, W. 1995, in *IAU Symp. 163, Wolf-Rayet Stars: Binaries, Colliding Winds, Evolution*, ed. K. A. van der Hucht & P. M. Williams (Dordrecht: Kluwer), 438